Contents lists available at ScienceDirect

Surfaces and Interfaces

journal homepage: www.sciencedirect.com/journal/surfaces-and-interfaces

Theoretical multiscale study on the properties, aqueous solution behavior and biological impact of zinc oxide nanoparticles

Nuria Aguilar [a], Sara Rozas [a], Elisabeth Escamilla [b], Carlos Rumbo [b], Sonia Martel [b], Rocío Barros [b], Pedro Angel Marcos [b,c], Alfredo Bol [b,c], Santiago Aparicio [*,a,c]

[a] Department of Chemistry, University of Burgos, Burgos 09001, Spain
[b] International Research Center in Critical Raw Materials for Advanced Industrial Technologies (ICCRAM), University of Burgos, Burgos 09001, Spain
[c] Department of Physics, University of Burgos, Burgos 09001, Spain

ARTICLE INFO

ABSTRACT

The aim of this theoretical study is to describe the relationship between the structure and the physicochemical properties of zinc oxide nanoparticles (ZnO NPs) and Mn doped ZnO NPs to assess their toxicological impact. In order to do so, a multiscale modelling approach is applied. Different nanoparticles, as well as the mechanism(s) of nanoparticle aggregation and growing, are characterized in terms of size and shape considering electronic, surface, structural and topological properties via quantum mechanics simulations. To evaluate the toxicology impact of ZnO NPs in human health safety and their possible environmental impact, classical molecular dynamics simulations were carried out to study the interaction between the nanomaterials and biological target systems: a set of selected human proteins and model plasma membranes. Likewise, the simulation of nanoparticles dispersion in aqueous media along with water adsorption on their surfaces was conducted.

The mayor findings may be summarized as: (*i*) the ZnO NPs from 12 to 96 (ZnO) units are characterized and their interaction energies, HOMO-LUMO gaps, superficial areas and volumes are reported; (*ii*) the $(ZnO)_{12}$ NP and $Zn_{11}MnO_{12}$ NP are further characterized via their topological properties, vibrational spectra, PDOS and non-covalent interactions; (*iii*) the doping with Mn atoms is favourable. The interaction energies, HOMO-LUMO orbitals and gaps, PDOS, atomic charges, superficial areas and volumes are reported for NPs doped with up to 5 Mn atoms; (*iv*) high water affinity for ZnO NPs is reported with both quantum and classical calculations, *v*) $(ZnO)_{12}$ NPs do not penetrate the cell membrane and (*vi*) the affinity energy of both ZnO and Mn doped NPs for human proteins is moderate.

The reported results provide in-depth whole-chain studies of zinc oxide nanoparticles, which have been successfully applied for different technologies.

1. Introduction

Nanomaterials [1] are currently used in many technologies, industries and science areas because of their unique and tuneable properties. Considering the chemical and physical diversity of the plethora of available and proposed nanomaterials, it is required to develop material structure–property–function relationship(s), which are needed to design materials for each specific application and which should be addressed applying different methodologies, i.e., theoretical and experimental studies to provide the required information that tackles with the complexity of the problem. From the point of view of in silico materials study and design, the use of a multiscale modelling approach allows a proper characterization of nanomaterials on different time and length scales. This may provide the required information for understanding the performance of the materials in terms of their physicochemical properties. In particular, Quantum Chemistry – based methods allow the exploration of these relationships in terms of electronic properties and are employed to characterise the nanomaterial and the interactions with other target materials or molecules from a nanoscopic perspective. Magnifying the scale, methods such as Molecular Dynamics simulations allow to characterize larger systems and predict phenomena for longer time scales such as the interaction of nanomaterials with target biological molecules, proteins and cell membranes, which can be used to predict their possible toxicological effects [2,3].

Zinc oxide (ZnO) is one of the most studied materials either in bulk or nanostructure forms [4]. Bulk ZnO adopts a wurtzite-type crystalline structure (hexagonal P63mc space group) at atmospheric pressure and room temperature. The unit cell contains two formula units of ZnO in which each zinc cation (Zn^{2+}) and oxygen anion (O^{2-}) are tetrahedrally coordinated to each other and stacked along the c-axis in alternating planess [5]. ZnO is a multitask II-IV n-type semiconductor with a direct band gap of 3.37 eV and an exciton binding energy of 60 meV [5,6]. The reported values of the exciton Bohr radius are between 1.8 and 2.8 nm [7] being the reported value for the bulk material 2.34 nm [8]. The physicochemical properties of ZnO such as chemical stability, biocompatibility and biosafety for bulk ZnO [9], high index of refraction, high electrical and phonon thermal conductivity, dipole-dipole structure for nanostructures, its photo-responsive nature to light in the UV region (< 400 nm) of spectrum, coupled with its abundance, low cost and easy synthesis process from bulk crystals to a large variety of nanomaterials come into a material applied in virtually every science field [9–16].

ZnO nanostructures are commercially available and are being synthesized with a myriad of methods: wet chemical, hydrothermal, sol-gel methods, atomic layer deposition, sputtering techniques, electrochemistry, inkjet printing and biological methods using microorganisms among others [17–22]. The physicochemical, optical and electronic properties exhibited by nanomaterials depends on their size, shape and aspect ratio. ZnO nanomaterials can be fabricated in different morphologies, e.g., nanoparticles (0D), nanotubes, nanowires, nanorods (1D and pseudo-1D), nanoplates, nanosheets (2D), nanoflowers, QDs and nanocrystals (3D) [8,18,23,24]. The high surface-to-volume ratio of nanostructures and the remarkable properties of ZnO mentioned above are responsible for the wide range of applications. Based on its high sensitivity and fast response, ZnO is used as gas sensor to detect CO_2, CO, O_2, NO_x, O_3, NH_3 and ethanol [10,16,25]. Similarly, ZnO is used as SERS substrate and applied to detect biological analytes like DNA, haemoglobin and others biomarkers [18]. The excellent sensory nature of metal oxides permits to develop sensors capable of detecting heavy metals [12,26] and drugs, in picomolar concentrations, such as antibiotics (azithromycin, clarithromycin and erythromycin [27]. In addition to its sensory role, ZnO is used as a filler to improve membrane performance to purify and decontaminate water and wastewater taking advantage of the outstanding photocatalytic activity of zinc oxide under UV light [17]. Focusing on its electron transport properties, ZnO is considered as a candidate for third generation solar cell technologies, and it is currently used as a blue-green led [6,8]. The piezoelectric behaviour of ZnO lead to commercialize piezoelectric nanogenerators [5] and its photoluminescence leads to develop scintillators [14]. Other ZnO applications vary from concrete and rubber additive, white pigment and heterogeneous catalysts for many chemicals to use as an ingredient in cosmetics and animal and human food [4,7,28]. One of the most relevant fields to make use of ZnO is biomedicine as this material presents antibacterial, anti-inflammatory and wound healing efficacy and is currently used as treatment for cancer and diabetes in photodynamic therapy [9,29].

ZnO nanoparticles (NPs) are being put to practical use in applications aforementioned, i.e., LEDs, solar cells, sensors and photocatalysts [30] and have been both experimental and theoretically studied reporting different morphologies as well as their electronic, optical, magnetic and structural properties. The ZnO NPs adopt different symmetries based on the number of atoms conforming the $(ZnO)_n$ nanocluster: for small clusters, $n < 8$, ring structures are the most stable conformations whereas for medium-size nanoclusters, $9 < n < 48$, the preferred configurations are hollow motifs as cages and tubes. For bigger clusters, $n > 48$, specifically $(ZnO)_{60}$ one, a sodalite-like structure, result of self-assembling $(ZnO)_{12}$ clusters, is the most energetically favourable [31–37]. Experimental time-of-flight mass spectroscopy results for ZnO NPs show relative abundance of clusters $(ZnO)_{34}$, $(ZnO)_{60}$ and $(ZnO)_{78}$ being the $(ZnO)_{60}$ the "magic" number NP due to its higher stability [38]. The $(ZnO)_{12}$ nanocluster has been theoretically evaluated with

quantum chemistry methods in terms of stability, energy, electronic and optical properties and sensory capacity for its pure and for metal and non-metal doped structures [39–44,15].

Considering the relevance of ZnO based nanoparticles, in spite of the collection of available studies and applications and the intrinsic interest of a safe by design approach, a whole study comprising and summarizing the physicochemical nature and properties of the materials, connected with their environmental behaviour (aqueous media) and their biological effects (toxicology) is still missing. Therefore, we report in this work a threefold *in silico* study (summarized in Fig. 1) with a multiscale materials modelling approach for the analysis and prediction of plain ZnO and Mn doped ZnO nanoparticle properties (using quantum chemistry methods based on Density Functional Theory, DFT), aqueous solution behaviour (via quantum chemistry and classical Molecular Dynamics, MD) as well as their interaction with model human proteins and model cell membranes (via MD simulations). The objectives of this work are: (*i*) to understand nanoparticle properties, (*ii*) to infer their possible mechanism(s) of aggregation, (*iii*) to study their solvation in aqueous environment and (*iv*) to predict their possible toxicological effects.

2. Methods

2.1. DFT calculations of nanoparticles

The initial structures for $(ZnO)_n$ nanoparticles (for $n = 12, 24, 36, 48, 60, 72, 84, 96$) were built with ABCluster 3.0 software [45], whereas the systems containing $(ZnO)_{12}$ nanoparticles with adsorbed or doped molecules (water and DPPC lipid) and atoms (Mn) were built using Avogadro program [46]. Self-consistent spin-polarized calculations were carried out to optimize the simulated systems for their energy and geometry structures with Dmol3 into Biovia Materials Studio software according to the Generalized Gradient Approximation (GGA) with the PBE functional [47] with DNP (Double Numerical plus polarization D-functions including a polarization *p*-function on all hydrogen atoms) basis set and the D3-Grimme's semiempirical correction [48] for taking into account the contribution of the long-range dispersion forces.

The binding energy, ΔE_{clean}, for clean $(ZnO)_n$ nanoparticles was calculated as follows:

$$\Delta E_{clean} = E_{(ZnO)_n} - n \cdot E_{Zn} - n \cdot E_O \tag{1}$$

where $E_{(ZnO)_n}$ stands for the energy of the optimized nanoparticle, E_{Zn} for the energy of the Zn atom and E_O for the energy of oxygen atom calculated at the same theoretical level. The binding energy for the nanoparticle doped with one Mn atom ($Zn_{11}MnO_{12}$) was calculated as follows:

$$\Delta E_{dopped} = E_{Zn_{11}MnO_{12}} - (11 \cdot E_{Zn}) - E_{Mn} - (12 \cdot E_O) \tag{2}$$

where $E_{Zn_{11}MnO_{12}}$ stands for the energy of the nanoparticle and E_{Zn}, E_{Mn} and E_O are the calculated energies of zinc, manganese and oxygen atoms respectively.

The interaction energy for $(ZnO)_n$ ($n = 24,48,72$) nanoparticles built from the assembling of $(ZnO)_{12}$ clusters for different interparticle orientation, with a total of 2, 4 or 6 $(ZnO)_{12}$ building blocks, was calculated as follows:

$$\Delta E_{assembling} = E_{(ZnO)_n} - x \cdot E_{(ZnO)_{12}} \tag{3}$$

where $E_{(ZnO)_n}$ stands for the energy of the system formed by $x = 2, 4$ or 6 $(ZnO)_{12}$ nanoparticles and $E_{(ZnO)_{12}}$ is the energy of the isolated $(ZnO)_{12}$ nanoparticle. Additionally, the binding energy of these systems was calculated using the Eq. (1).

The binding energy for the water molecule, DPPC molecule and Mn atom adsorbed onto the $(ZnO)_{12}$ nanoparticle was calculated in the following way:
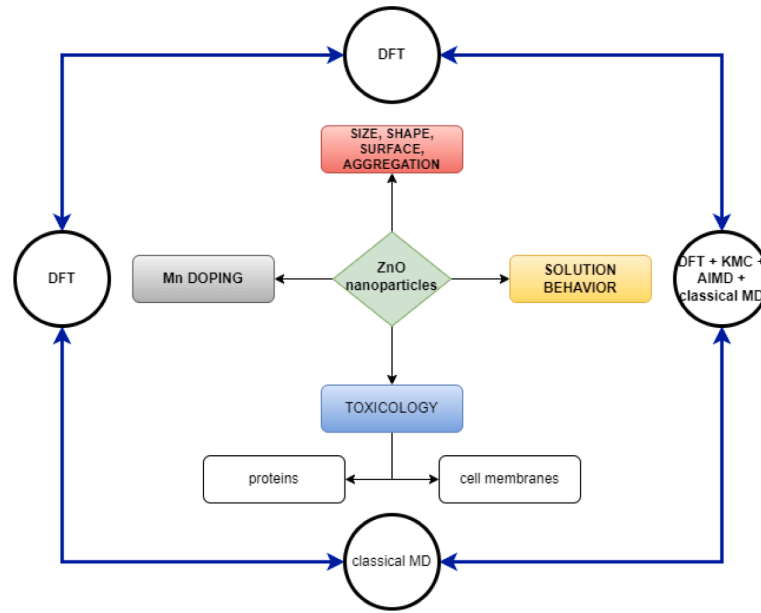
Fig. 1. Scheme of the multiscale materials modelling approach considered in this work.

$$\Delta E_{H_2O} = E_{(ZnO)_{12}/H_2O} - E_{(ZnO)_{12}} - E_{H_2O} \tag{4}$$

$$\Delta E_{DPPC} = E_{(ZnO)_{12}/POPC} - E_{(ZnO)_{12}} - E_{DPPC} \tag{5}$$

$$\Delta E_{Mn} = E_{(ZnO)_{12}/Mn} - E_{(ZnO)_{12}} - E_{Mn} \tag{6}$$

where $E_{(ZnO)_{12}/H_2O}$, $E_{(ZnO)_{12}/Mn}$ and $\Delta E_{DPPC}$are the energies reported for the whole systems, $E_{(ZnO)_{12}}$ is the energy for the $(ZnO)_{12}$ nanoparticle and E_{H_2O}, E_{DPPC} and E_{Mn} are the energies for the water molecule, DPPC molecule and Mn atom, respectively.

The binding energy for the interaction of one endohedral water molecule with the $(ZnO)_{12}$ nanoparticle was calculated as follows:

$$\Delta E_{endoH_2O} = E_{(ZnO)_{12}/endoH_2O} - 12 \cdot E_{Zn} - 12 \cdot E_O - E_{H_2O} \tag{7}$$

where $E_{(ZnO)_{12}/endoH_2O}$ stands for the energy of the whole system and E_{Zn}, E_O and E_{H_2O} are the reported energies for zinc and oxygen atoms and water molecule.

In order to take into account the difference between the formation energy for the $(ZnO)_{12}$ nanoparticle with and without one endohedral water molecule ($\Delta E_{(ZnO)_{12}endo}$ and ΔE_{clean}, respectively), the endohedral water molecule of the previous optimized system was removed and a single point energy calculation was carried out with the $(ZnO)_{12}$ nanoparticle to calculate the binding energy for the geometry of the endohedral nanoparticle as follows:

$$\Delta E_{(ZnO)_{12}endo} = E_{(ZnO)_{12}/endo} - 12 \cdot E_{Zn} - 12 \cdot E_O \tag{8}$$

where $E_{(ZnO)_{12}/endo}$ stands for the energy of the $(ZnO)_{12}$ nanoparticle without the water molecule while preserving the geometry of the endohedral system andE_{Zn} and E_O are the reported energies for zinc and oxygen atoms. The formation energy for the $(ZnO)_{12}$ clean nanoparticle was calculated via Eq. (1). The difference between those binding energies was calculated as follows:

$$\Delta E_{(ZnO)_{12}endo/clean} = \Delta E_{(ZnO)_{12}endo} - \Delta E_{clean} \tag{9}$$

Topological analysis of the optimized geometries for $(ZnO)_{12}$ and $Zn_{11}MnO_{12}$ nanoparticles were carried out with Multiwfn software [49]. This analysis was applied according to the quantum theory of atoms-in-molecules (QTAIMs) [50] in which the interaction regions are characterized by bond and ring critical points (BCPs and RCPs respectively) and their corresponding values of electron density (ρ) and Laplacian of electron density ($\nabla^2\rho$). Further analysis was carried out by Non-Covalent Interaction (NCI) to display the strength and nature of interatomic and intermolecular interactions. Atomic charges inferred from Mulliken charges were obtained from DFT simulations of the aforementioned nanoparticles. Properties of the nanoparticles, such as Density of States (DOS), Raman and vibrational spectrum, HOMO-LUMO, deformation electron density and electrostatic potential were calculated with Dmol3 in Biovia Materials Studio.

2.2. DFT – tight binding simulations

Density Functional Theory - Tight Binding (DFT-TB) method solves the Kohn-Sham equations using Slater-Koster parameters, derived from DFT calculations. This methodology has been applied to simulate Ab Initio Molecular Dynamics (AIMD) adsorption of different molecules onto ZnO, ZnO-modified surfaces NPs [51–53]. Saeedimasine et al. used DFTB as the standard method to compute Lennard-Jones parameters for developing classical molecular dynamics force fields for ZnO and to compare the results of DFTB AIMD and MD simulations [54].

Calculations using DFT-TB scheme were used in this work for several purposes. This kind of calculations were done with DFBT+ code [55] into Biovia Materials Studio using Slater-Koster set from znorg library [56]. Tolerance for calculations self-consistency was set to 10^{-6}. The k-points meshes corresponded to a $4 \times 4 \times 4$ distribution. Five families of DFT-TB based simulations were carried out:

(i) unit cell for the crystal structure of ZnO wurzite was obtained from MaterialsProject database [57], and reoptimized using DFT-TB, leading to lattice constants of $a = 3.25$ Å and $c = 5.21$ Å in suitable agreement with literature information: 28 DFT – based approaches give as average results $a = 5.235$ Å and $c = 5.209$ Å [58], thus confirming the suitability of DFT-TB for describing ZnO properties. Surfaces were created from this crystal structure cleaving through relevant planes defined by the corresponding Miller indices, thus the surface energy, $E_{surface}$, was calculated according to Eq. (8):

$$E_{surface} = \frac{\left(E_{slab} - \frac{N_{slab}}{N_{bulk}} \cdot E_{bulk} \right)}{2A_{slab}} \tag{10}$$

where E$_{slab}$ stands for the energy of relaxed surface slabs, E$_{bulk}$ is the

energy of the bulk unit cell, N_{slab} is the number of the ZnO units in surface slab, N_{bulk} is the number of the ZnO units in the unit cell and A_{slab} is the surface area. From the $E_{surface}$ value a Wulff model nanoparticle for ZnO was built using WulffPack [59].

(ii) the removal of Zn atoms from ZnO surfaces was calculated using DFT-TB. The corresponding energy barriers were also obtained as the difference between the energy of the system with a Zn atom at a distance d of the initial, not removed position, and the energy of the corresponding unperturbed surface.

(iii) the adsorption and interaction of liquid water on ZnO surfaces was studied by building a $5 \times 1 \times 1$ Å^3 supercell from the previously optimized structures for each surface and a water layer (density = 1 g cm^{-3}) was placed on top of each. The evolution of the systems was studied using *ab initio* MD simulations (AIMD) with DFT-TB. 50 ps AIMD simulations were developed in the NPT ensemble at 308 K and 1 bar controlling temperature and pressure with the Nosé–Hoover thermostat and Berendsen barostat, respectively.

(iv) the solvation of (ZnO)$_{12}$ nanoparticle with water molecules was also studied by AIMD DFT-TB simulations by placing a previously built (ZnO)$_{12}$ unit into a cubic simulation box with $20 \times 20 \times 20$ Å^3 filled with water molecules at a density = 1 g cm^{-3}. 50 ps AIMD NPT simulations at 308 K and 1 bar were carried out using the same approach as for water interaction with surfaces.

(v) the interaction of (ZnO)$_{12}$ nanoparticles with model plasma membranes has been calculated through coarse grained MD simulations to study its possible biological (toxicological) impact. To this end a suitable force field parameterization was developed using DFT-TB calculations selecting the DPPC lipid as a model constituent of eukaryotic cell membranes. The interaction between this lipid and (ZnO) molecule, as the building unit of (ZnO)$_{12}$ nanoparticle, was characterizied considering the structural moieties of the lipid: choline, phosphate, glycerol and alkyl chain, modelled as a butane molecule. The interaction of the lipid with ZnO was quantified via DFT-TB as a function of their separation, and for these results the corresponding force field parameters according to the Martini CG force field [60] were obtained, thus, allowing the CG-MD study of nanoparticles–plasma membranes interaction.

2.3. All atom classical MD simulations of nanoparticles in water

Simulations for (ZnO)$_{12}$ nanoparticles in water solution were carried out using Biovia Materials Studio – Forcite according to the COMPASSIII forcefield [61]. Initial boxes containing from 1 to 12 (ZnO)$_{12}$ nanoparticles in a $50 \times 50 \times 50$ Å^3, also filled with water molecules to density 1 g cm^{-3} were built. NPT simulations for 50 ns, with 1 fs timestep, at 308 K and 1 bar were carried out considering the Nosé thermostat and Berendsen barostat.

2.4. Coarse grained MD simulations of nanoparticles – plasma membranes interactions

The possible biological effect of (ZnO)$_{12}$ structures were addressed through the study of nanoparticles with model plasma membranes. CG-MD simulations were carried out with Mesocite – Biovia Materials Studio using Martini force field parameterization as well as the parameters for the nanoparticle–lipid interactions as inferred from DFT-TB calculations explained in the previous section. The involved molecules and their CG description is as follows: (*i*) (ZnO)$_{12}$ is described as a unit formed by twelve (ZnO) molecules; (*ii*) water molecules are described as a four water molecules bead, i.e., each water bead representing four water molecules; (*iii*) DPPC lipid is described as the combination of eight beads: one choline bead + one phosphate bead + two glycerol beads + four alkyl sites, each representing 4 carbon atoms. Coarse grained MD simulations with the selected DPPC lipid were performed in the common form used to study biomembranes for toxicological purposes [62]. A lipid bilayer formed by 63 lipids per leaflet was hydrated with 1000

water beads, i.e., 4000 water molecules, on each side, thus leading to a 63:5 water to lipid ratio. Simulations of clean water – lipid bilayer were carried out for reference purposes. The interaction of (ZnO)$_{12i}$, $i = 1$, 3 or 6 nanoparticles with the lipid bilayer – water system was studied placing them on one side of the bilayer to mimic inner and outer sides of plasma membranes. A 1.5, 4.5 and 8.5 wt% content of nanoparticles has been swept with this strategy. CG-MD simulations were carried out with a two stages procedure: (*i*) 1 ns NVT set of simulations at 328 K for equilibration purposes followed by (*ii*) 1000 ns NPT simulations at 328 K and 1 bar. The selected temperature is above the phase transition temperature for DPPC bilayers (315 K [63]), thus assuring the bilayer being in physiological conditions. Temperature and pressure were controlled with Nosé thermostat and Berendsen barostat, respectively, with 1.0 ps for coupling constants of the thermostat and barostat along all the simulations. Likewise, 20 fs time step was used for all the simulations.

2.5. Protein docking of nanoparticles

A set of 102 human proteins, covering different families to infer possible mechanisms of interactions, were selected for docking calculations with (ZnO)$_{12}$, Zn$_{11}$MnO$_{12}$, Zn$_7$Mn$_5$O$_{12}$ and (MnO)$_{12}$ nanoparticles. All the protein structures were obtained from the Protein Databank, with the structure for both proteins and nanoparticles, were prepared with PlayMolecule - ProteinPrepare: a protein preparation app for MD simulations – [64] and Autodock Tools with Gasteiger charges considered for all the aforementioned systems. The *rigid ligand* and *rigid receptor docking* calculations were carried out with Autodock Vina [65] using the AutoDock4$_{Zn}$ v1.2.3 implemented force field [66].

3. Results and discussion

3.1. Properties of neat ZnO nanoparticles

In a first stage of the research, the properties of (ZnO)$_n$ nanoparticles were calculated as a function of n with n ranging from 1×12 to $8 \times 12 = 96$, Fig. 2a to h. The smallest studied nanoparticle ($n = 1 \times 12$) agrees in shape, geometry and properties with results in literature [39], forming pseudospherical structure with 8 hexagonal and 6 square faces. This nanoparticle has a 2.58 eV HOMO-LUMO gap, which precludes a semiconducting behaviour but leading to a band gap lower than e.g. the value obtained for (ZnO) wurtzite – like structure that has a 3.37 eV band gap [67]. This result is in line with the well-known band gap underestimation by GGA - PBE DFT calculations. For correcting this underestimation, band gap calculations on (ZnO)$_{12}$ optimized nanoparticle were carried out considering Hubbard method ($U_d = 9.5$ eV for Zn atoms and $U_p = 7.86$ eV for O atoms [68]), that predicts a HOMO-LUMO gap of 3.98 eV, i.e. and underestimation of 1.4 eV with non-corrected GGA-PBE predictions), which is close to the experimental value for ZnO – wurtzite structure. As the nanoparticle size increases, structures comprising squared, hexagonal and octagonal faces are formed, whereas for $n > 5 \times 12 = 60$ core – shell structures are formed, see panels f, g and h of Fig. 2. For all the considered structures, highly stable nanoparticles are inferred as confirmed by the large ΔE values. The evolution of the binding energy ΔE with n follows a linear pattern. That is to say, in spite of the very different geometries, the particle evolution is characterized by the aggregation of building (ZnO) units, Fig. 2i. Nevertheless, a more detailed analysis of ΔE as a function of the number of (ZnO) units (n), Fig. 2j, indicates that as n grows the contribution of each (ZnO) unit also increases (larger $\Delta E \times n^{-1}$) but reaching an asymptotic behaviour towards 7.3 eV per (ZnO) for $n > 60$, which corresponds to the starting of forming core – shell configurations. Likewise, the evolution of the HOMO-LUMO gap with nanoparticle size is reported in Fig. 2k. This shows a non – linear decrease approach to an asymptotic value of roughly 1.7 eV again for $n > 12 \times 5 = 60$, i.e., the larger the particles, the lower the HOMO-LUMO gap but leading to a constant gap value for larger nanoparticles.
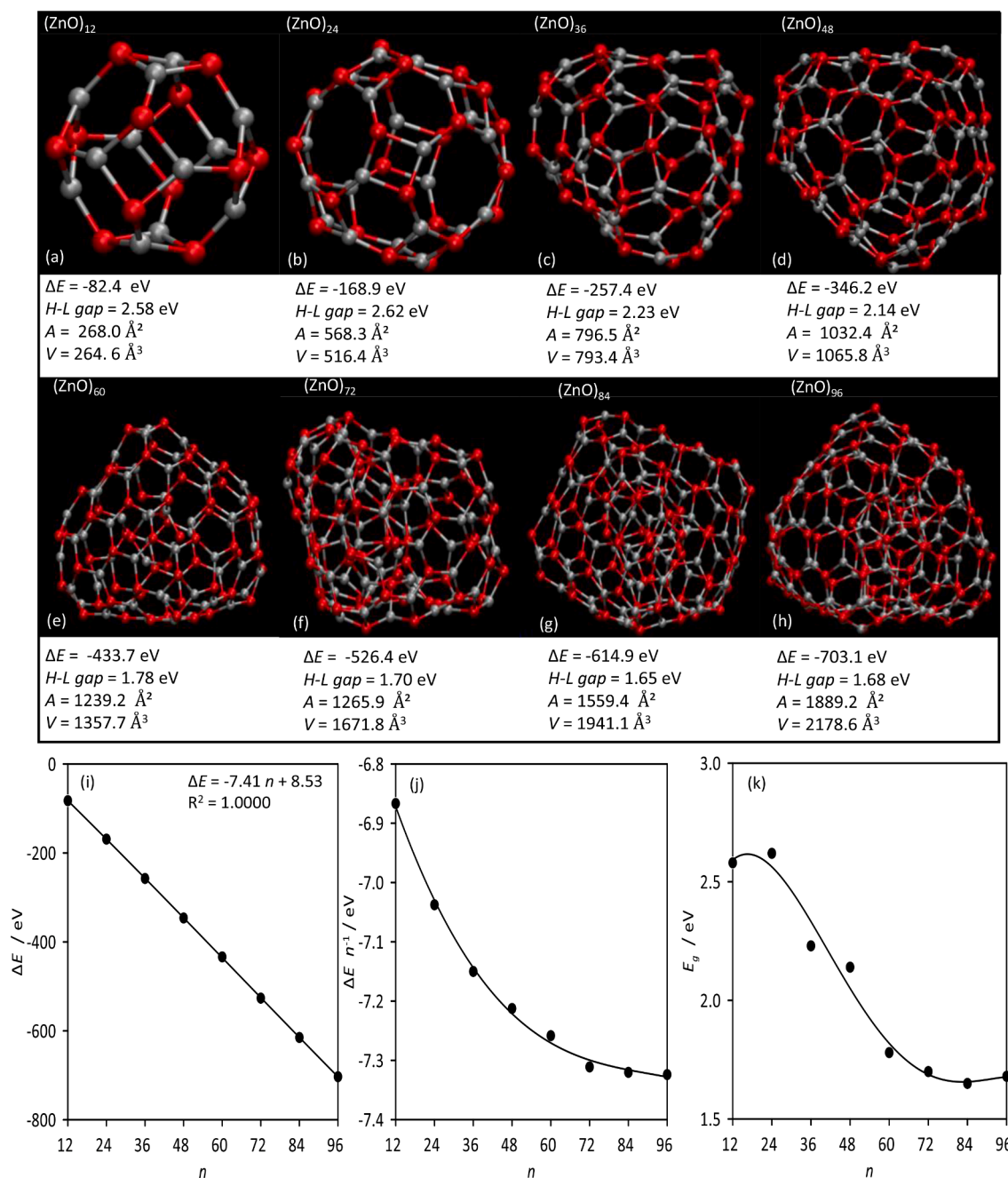
Fig. 2. DFT optimized structures of $(ZnO)_n$ nanoparticles reporting binding energy, ΔE, HOMO - LUMO gap, *H-L gap*, surface area, *A*, and nanoparticle volume, *V*. Atom color code: (red) oxygen, (gray) zinc.

Further analysis of $(ZnO)_{12}$ nanoparticle properties were carried out through the prediction of Raman and vibrational spectra, Fig. 3a and b. The Raman spectra of the considered nanoparticle is in suitable agreement with experimental ones for 5 nm diameter nanoparticles [69] although with peak shifting because of the 0.64 nm diameter for $(ZnO)_{12}$ nanoparticles considered in Fig. 3. Korepanov et al. [70] reported a Raman width broadening and peak shifting on going to subnanometric ZnO nanoparticles but maintaining the main Raman features, thus justifying Raman comparison among $(ZnO)_{12}$ and larger nanometric particles. Seven main peaks are inferred from the Raman spectra at 70, 95, 169, 203, 361, 407 and 630 cm^{-1}. Experimental literature data for (ZnO) nanoparticles [71] indicate six Raman active phonon modes at 101 (E_2(low)), 381 (A_1(TO)), 407 (E_1(TO)), 437 (E_2(high)), 574 (A_1(LO)) and 583 (E(LO)) cm^{-1}. The 437 cm^{-1} corresponding to the E_2(high) high Raman mode is dominantly assigned to the oxygen

vibration [65,72], which is typical characteristic of the hexagonal wurtzite ZnO and, in addition, the intensity of this peak increases with nanoparticle size and also its frequency decreases with nanoparticle size, i.e., small nanoparticles as the $(ZnO)_{12}$ one should present a weaker peak at frequencies lower than 437 cm^{-1}. This behaviour is confirmed by the E_2(high) obtained for $(ZnO)_{12}$ nanoparticle at 407 cm^{-1}, i.e., a 30 cm^{-1} redshifting in comparison with larger nanoparticles. The remaining peaks for $(ZnO)_{12}$ nanoparticle in Fig. 3a appear at different frequencies to those reported for larger particles in the literature, confirming the different structure for small nanoparticles in comparison with larger ones, that are closer to the characteristics of wurtzite – like crystal structures. For the vibrational spectrum, four main peaks are inferred, corresponding to displacement vectors reported in Fig. 3b. These vibrational features correspond to stretching vibrations of Zn – O bond.

The characterization of $(ZnO)_{12}$ nanoparticle is reported in Fig. 4.
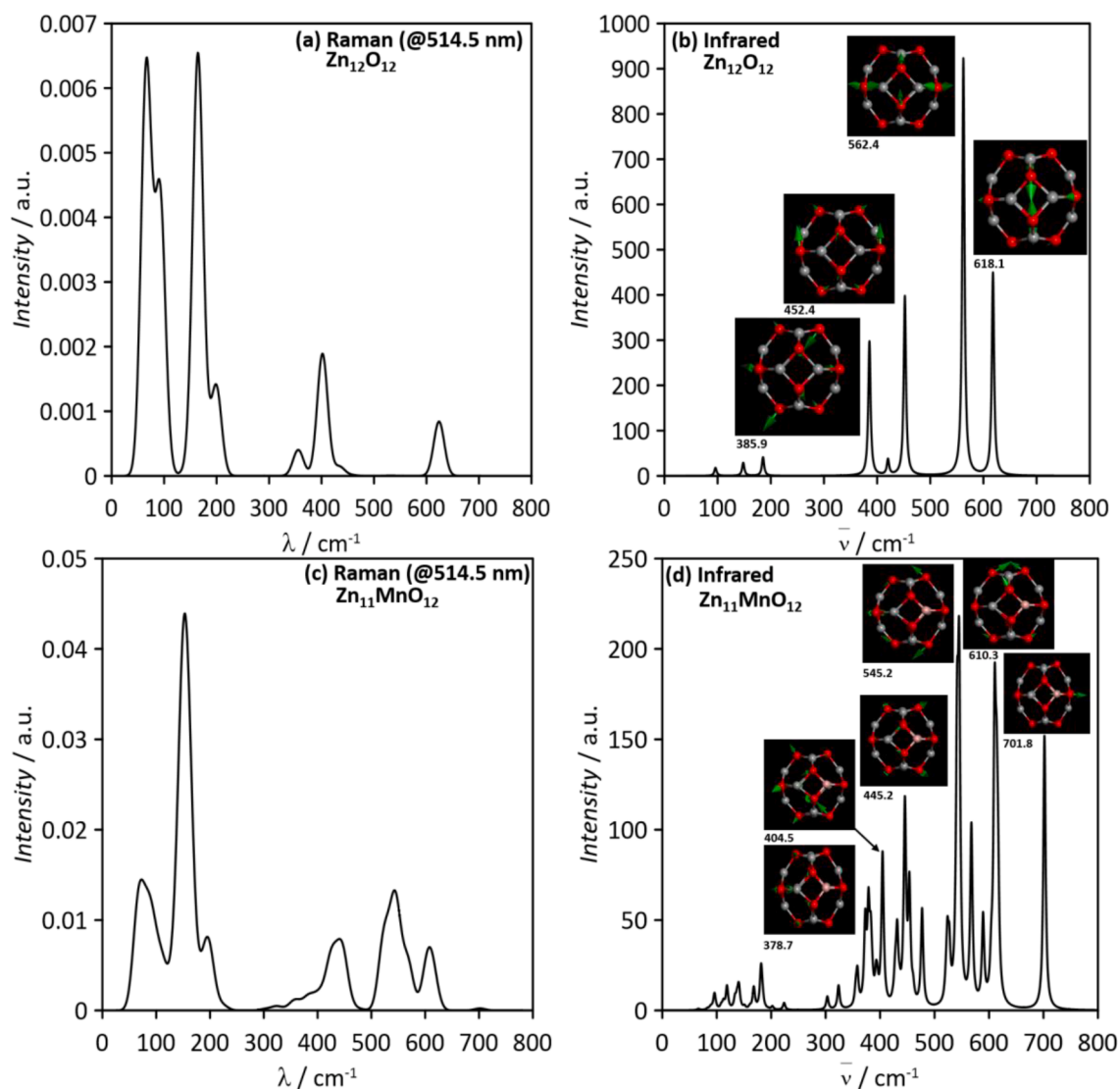
Fig. 3. DFT calculated Raman and infrared (vibrational) spectra of (ZnO)$_{12}$ (Fig. 2a) and (Zn$_{11}$MnO$_{12}$) nanoparticles The main vibrational modes are indicated in panel (b) with the corresponding displacement vectors. Atom color code: (red) oxygen, (gray) zinc, (pink) manganese.

The first feature observed in Fig. 4a is the difference between Zn-O bond lengths. Bonds in the squared faces of the nanoparticle are 0.09 Å larger than those in the hexagonal ones, explaining the different Zn – O vibrations as reported in Fig. 3b. The significant difference in the extent of the angles formed by adjacent bonds, lower for the Zn – O – Zn than for the O – Zn – O, leads to non – regular faces with the disruption induced by oxygen atoms. The deformation electron density and the corresponding Mulliken charges reported in Fig. 4b indicate largely localized charge centers with +/- 0.86 charges for Zn / O atoms, showing the charge transfer from Zn to O atoms, in agreement with values for very small ZnO nanoclusters, e.g. (ZnO)$_4$ [73], and larger nanoparticles [74]. Regarding the frontier orbitals, HOMO orbital (Fig. 4c1) has antibonding nature, and it is formed by the combination of 2p orbitals from O and 3d from Zn, with main contribution from O atoms, and thus, it is mainly located onto every O atom. The LUMO orbital, Fig. 4c2, is also mainly located on O atoms and, although previous results for larger nanoparticles indicated that LUMOs for (ZnO) nanoparticles are composed of 4 s Zn atomic orbitals [69], our results show that they are mainly located on O atoms instead of Zn ones.

The topological analysis of bonding of (ZnO)$_{12}$ nanoparticle was carried out according to Non-Covalent Interactions (NCI) and QTAIM and reported in Fig. 4d and e. The NCI analysis shows steric effects

largely different for squared and for hexagonal faces but all of them with face – centered spots, therefore showing very different mechanisms of Zn – O bonding depending on the face position. Likewise, the large symmetry of the particle is confirmed by the development of an NCI (green) spot at the nanoparticle center, which confirms interatomic interactions beyond those atoms in the same face, thus contributing to the cage stabilization. Regarding QTAIM analysis, the properties of the nanoparticle are analyzed through the formation of critical points (bond, BCP, and ring, RCP) considering the values of the electron density, ρ, and the corresponding Laplacian density, $\nabla^2\rho$, at these points. Results in Fig. 4e show the formation of BCPs along all the Zn – O bonds as well as RCPs at the center of squared and hexagonal faces. Nevertheless, the properties of BCPs depend on the face type, with larger values for hexagonal faces, i.e., indicating stronger Zn – O covalent bonds for atoms in hexagonal faces, in agreement with shorter bond distances as reported in Fig. 4a. Likewise, the large $\nabla^2\rho$ values point to highly polarized bonds, thus resulting in Zn to O charge transfer as quantified by the Mulliken charges reported in Fig. 4b. Moreover, the formation of RCPs at the faces centers indicates interatomic interaction beyond direct Zn – O covalent bonding, thus contributing to the nanoparticle stabilization, but these RCPs are stronger for squared centers, leading to more efficient interatomic interactions, in agreement with the shape of the interacting
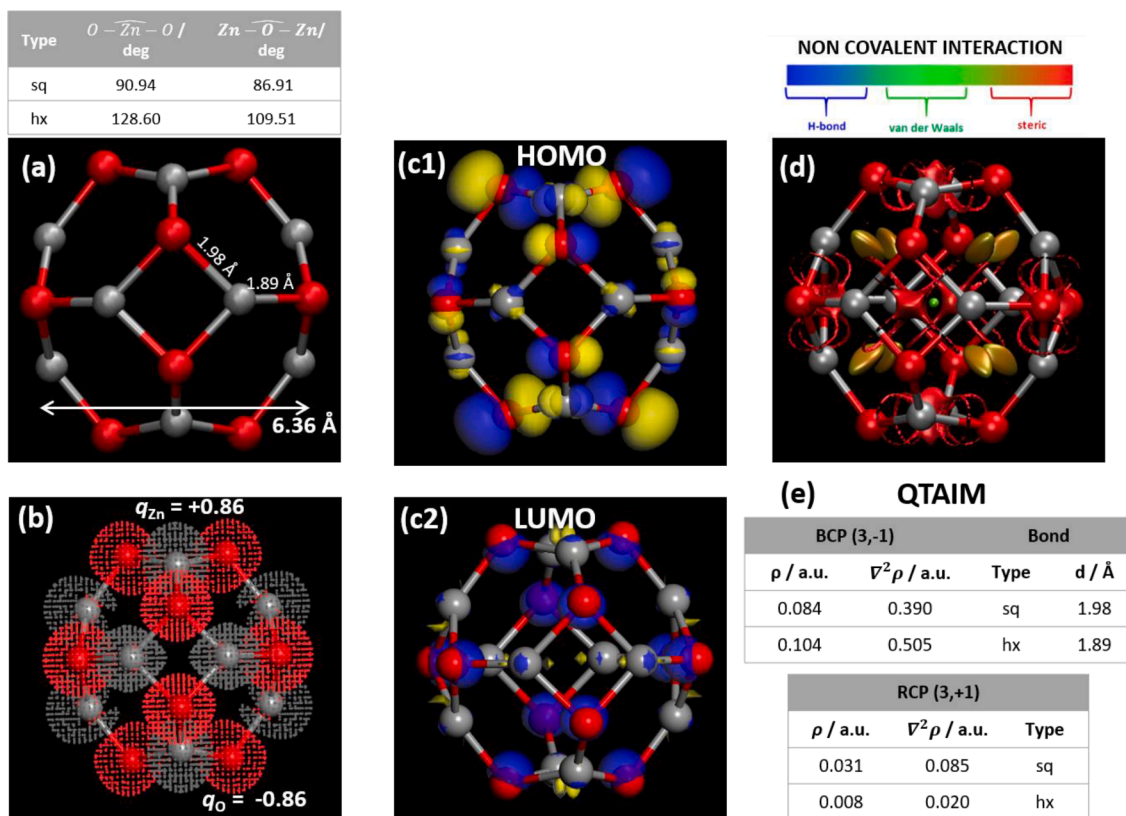
Type	$O - \widehat{Zn} - O$ / deg	$Zn - \widehat{O} - Zn$ / deg
sq	90.94	86.91
hx	128.60	109.51

(e) QTAIM

BCP (3,-1)		Bond	
ρ / a.u.	$\nabla^2\rho$ / a.u.	Type	d / Å
0.084	0.390	sq	1.98
0.104	0.505	hx	1.89

RCP (3,+1)		
ρ / a.u.	$\nabla^2\rho$ / a.u.	Type
0.031	0.085	sq
0.008	0.020	hx

Fig. 4. DFT calculated properties of $(ZnO)_{12}$ nanoparticle: (a) geometrical properties, (b) deformation electron density and Mulliken atomic charges, (c) frontier orbitals, (d) NCI analysis and (e) QTAIM analysis. Atom color code: (red) oxygen, (gray) zinc.

regions as inferred from NCI analysis in Fig. 4d.

Additional analysis of nanoparticle electronic properties was carried out through Density of States (DOS) for small $(ZnO)_{12}$ and larger $(ZnO)_{60}$ nanoparticles, Fig. 5. Total DOS show minor changes as nanoparticle size increases, the main feature resulting in a decrease in HOMO – LUMO gap, as shown in Fig. 2. The main changes upon nanoparticle size increase stands on the region above LUMO orbital. This may be justified considering the formation of core – shell structure for $(ZnO)_{60}$ in comparison with the hollow one for $(ZnO)_{12}$, which would lead to a more efficient overlapping of orbitals giving rise to a more compact orbital

distribution for the core-shell structure and resulting in a lower separation between orbitals above the LUMO level. This effect is confirmed by the corresponding partial DOS (PDOS), which shows almost negligible difference up to HOMO frontier orbital but changes for orbitals above LUMO level, especially considering *s* and *p* atomic orbitals contributions.

3.2. Growing of neat ZnO nanoparticles though $(ZnO)_{12}$ aggregation

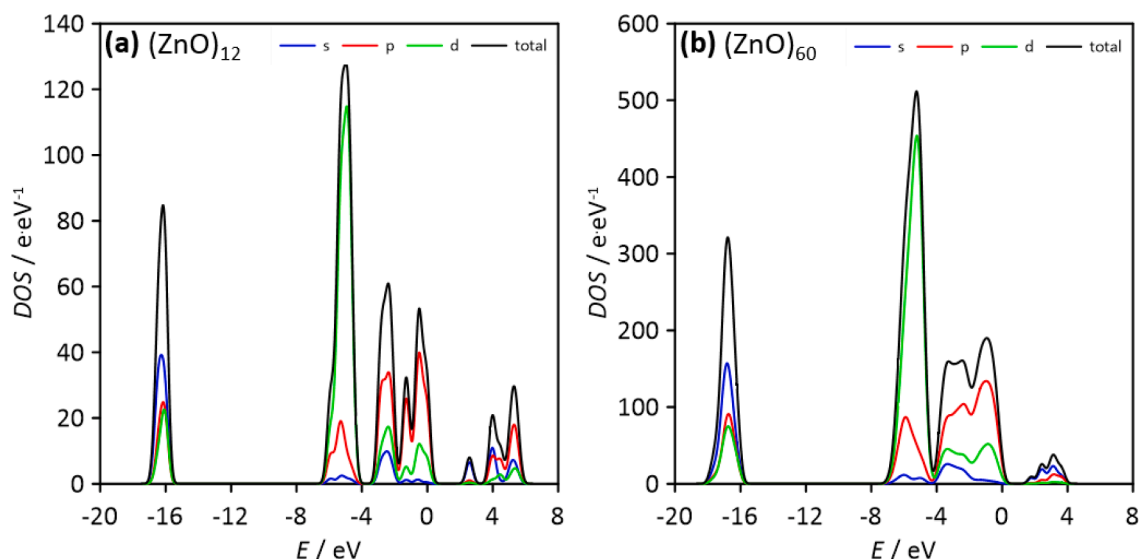The mechanisms of nanoparticle aggregation and its growing was

Fig. 5. DFT calculated total and partial density of states for (a) $(ZnO)_{12}$ (Fig. 2a) and (b) $(ZnO)_{60}$ (Fig. 2e) nanoparticles.

studied considering $(ZnO)_{12}$ as a model. Results reported in Fig. 6 consider assembly of 2, 4 and 6 nanoparticles to study possible sequential aggregation. For the two-particles case, Fig. 6a, considering the presence of two types of faces in the nanoparticle (squared and hexagonal), three types of interactions are possible: (*i*) squared to squared, (*ii*) hexagonal to hexagonal and (*iii*) squared to hexagonal. The three types of interactions lead to the formation of rod – like structures with large binding energies, although stronger interactions being inferred for hexagonal-hexagonal (-4.7 eV) than for squared-squared (-3.6 eV) or squared–hexagonal interactions (-2.9 eV) but confirming in all the cases the stabilization through aggregation. The Zn – O new bonds upon nanoparticle aggregation are 2.01 – 2.02 Å long, only slightly larger than those in the original nanoparticle (Fig. 4a), which shows that aggregation mechanism is based on the formation of new covalent bonds. It should be remarked that the pairing of $(ZnO)_{12}$ leading to the formation of rod – like nanoparticles with $n = 24$ gives rise to a total interaction energy of -168.4 eV, that is almost equal to the reported interaction energy for the hollow $n = 24$ nanoparticle shown in Fig. 2b (-168.9 eV). This fact points to the feasibility of the production of rod–like nanoparticles through aggregation of $(ZnO)_{12}$ as a reliable mechanism of growing, resulting in nanoparticles with similar energies to those of hollow nanoparticles. It should be remarked that the rod – like nanoparticles ($n = 24$) reported in Fig. 6a do not evolve to the hollow ones reported in Fig. 2b, which can be justified considering the equal energies, i.e., stability, and the possible large energy barriers for evolving from the rod – like structures to hollow ones.

3.3. Growing of neat ZnO nanoparticles: $(ZnO)_{12}$ aggregation vs. atomic aggregation

Additional growing was studied from the rod – like structures by the addition of two new $(ZnO)_{12}$ nanoparticles at different positions as shown in Fig. 6b. These two growing patterns lead to star–shaped and zig–zag planar structures with large interparticle interaction energies and also large total interactions energies, thus confirming stable structures through aggregation for $n = 48$. Likewise, the comparison of the properties for the particles with $n = 48$ obtained by aggregation in Fig. 6b with those for the hollow compact nanoparticle in Fig. 2d points to almost equal total interaction energy (roughly 1.52 eV lower in absolute value for those grown from atomic aggregation), thus showing the possibility of formation of both nanoparticles. Further growing to $n = 72$ through $(ZnO)_{12}$ addition is displayed in Fig. 6c. Again, structures with

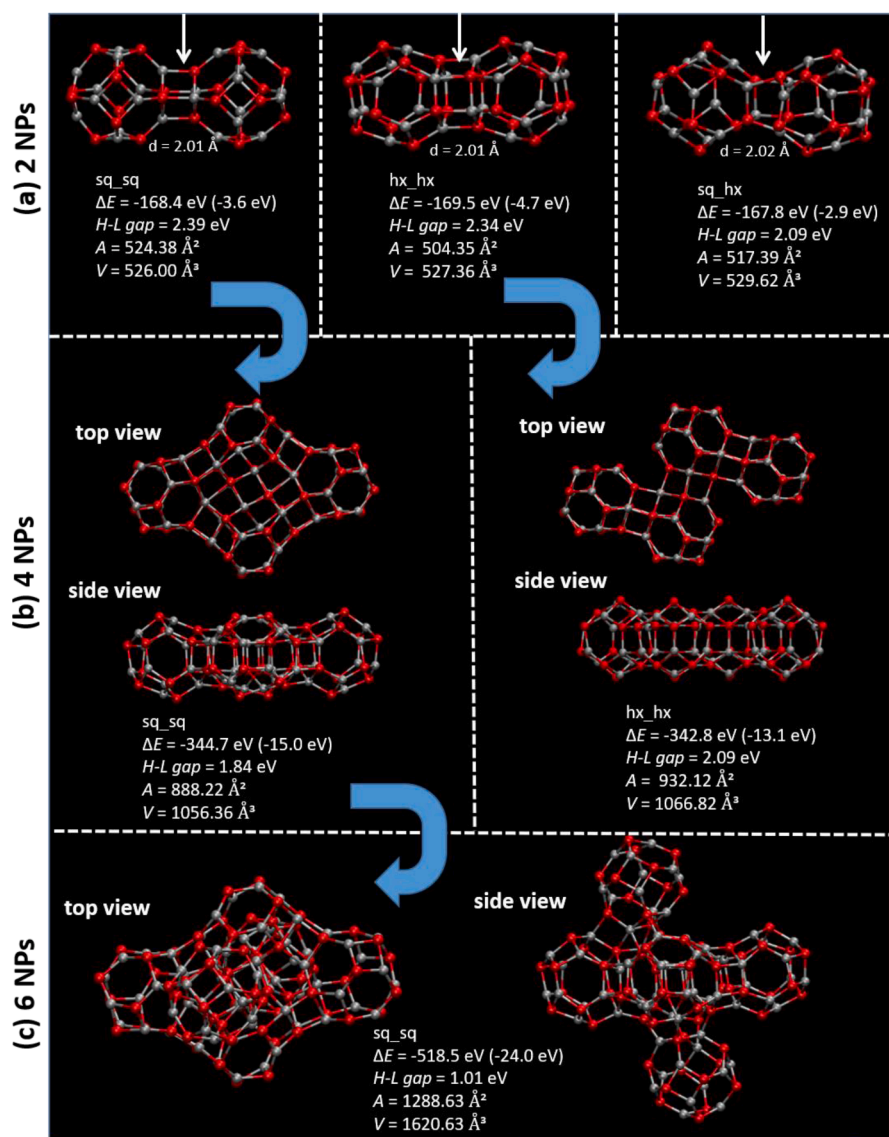**Fig. 6.** DFT results for the self-aggregation of $(ZnO)_{12}$ nanoparticles (Fig. 2a) considering different mechanisms of aggregation and increasing number of nanoparticles. Atom color code: (red) oxygen, (gray) zinc.

less compact shape and different geometry from the one reported in Fig. 2f are confirmed, with analogous stabilization effects, being 8 eV more stable the core – shell nanoparticle depicted in Fig. 2f. Therefore, the growing mechanism via $(ZnO)_{12}$ aggregation explored in Fig. 6 indicates the formation of stable structures with shapes very different to those formed via atomic addition (Fig. 2). Final structures ending both growing routes have very similar energies, slightly more stable the more compact ones, with topologies and geometric properties (surface area and nanoparticle volume) also quite similar. As a partial conclusion, it can be established the role of $(ZnO)_{12}$ magic number nanoparticles as seed for ZnO nanoparticle growing.

3.4. Mn adsorption and doping of ZnO nanoparticles

The modification of (ZnO) nanoparticles with Mn atoms was analyzed considering two possible mechanisms using $(ZnO)_{12}$ as model nanoparticle: (*i*) Mn atoms adsorption on nanoparticle surface and (*ii*) $(ZnO)_{12}$ substitutional doping with Mn atoms. Results for the adsorption of a single Mn atom on $(ZnO)_{12}$ nanoparticle are reported in Fig. 7. Six different initial possible adsorption sites on the nanoparticle surface were considered, but after optimization all of them converged to only two possible adsorption configurations, with Mn atoms placed and bonded above two neighbor atoms from initial hexagonal faces. This mechanism of adsorption involves the replacement of an oxygen atom from hexagonal faces vertex, thus O moving out of nanoparticle surface, being replaced by Mn atoms. In both cases the Mn adsorption leads to a large disruption of the nanoparticle geometry, obtaining a non-spherical nanoparticle largely disrupted in the Mn adsorption region. In spite of the nanoparticle disruption upon Mn adsorption, the calculated adsorption energies (1.86 and 1.68 eV) show a favorable adsorption process. The Mn – Zn bond lengths are roughly 2.5 Å, whereas the Mn – O is roughly 1.7 Å, remarkably shorter than the Zn – O ones (1.9 to 2.0 Å), thus suggesting stronger covalent bonds in the nanoparticle for Mn

sites. These strong Mn – Zn (through the formation of two bonds) and Mn – O bonds would be the reason of the nanoparticle disruption after Mn adsorption. The main changes in the electronic properties of the nanoparticle after Mn adsorption result in the decrease of the HONO-LUMO gap evolving from 2.58 eV (not Hubbard corrected) to 0.73 or 0.59 eV, as a result of the changes in DOS (Fig. 7) because of the Mn *d* orbitals (PDOS in Fig. 7). Therefore, the modification of $(ZnO)_{12}$ nanoparticles via single atom Mn adsorption is highly favored process leading to remarkable changes in nanoparticle properties

A second type of (ZnO) nanoparticles modification was studied through the Mn doping giving rise to nanoparticles with $(Zn_{12-n}Mn_nO_{12})$ stoichiometry obtained by increasing doping of neat $(Zn_{12}O_{12})$ nanoparticles. Doping in the $n = 1$–5 range as well as neat $(Mn_{12}O_{12})$ nanoparticles were studied, Fig. 8. First, the comparison of the properties for $(Zn_{12}O_{12})$ and $(Mn_{12}O_{12})$ nanoparticles, i.e., properties of neat Zn and Mn nanoparticle oxides, show that both nanoparticles have similar geometries: hexagonal and squared faces are formed and, in both cases, the pseudospherical structure of the nanoparticle is obtained. With regard to the stabilization energy related to the formation of the nanoparticles and Zn substitution, values for the energy of formation of $(Mn_{12}O_{12})$ nanoparticle is remarkably larger than the same magnitude for $(Zn_{12}O_{12})$. Consistently, the doping of $(Zn_{12}O_{12})$ with Mn atoms (i.e., increasing n in $Zn_{12-n}Mn_nO_{12}$) leads to nanoparticle stabilization, Fig. 8a, i.e., Mn doping would be a highly favourable process. Likewise, although the shapes of both $(Zn_{12}O_{12})$ and $(Mn_{12}O_{12})$ are equivalent, results in Fig. 8b indicate that neat $(Mn_{12}O_{12})$ is larger in volume and surface than $(Zn_{12}O_{12})$. Nevertheless, the effect of doping, i.e., increasing n on $Zn_{12-n}Mn_nO_{12}$ for the size and surface of the nanoparticle is clearly non – linear (Fig. 8b) showing subtle and very minor changes for $n < 5$, therefore, the main geometrical properties of the $Zn_{12}O_{12}$ nanoparticles are not largely changed upon Mn doping. Regarding the atomic charges, Fig. 8c, results confirm very minor changes for Mn doping for $n < 5$, with Zn and O atom charges being independent of Mn
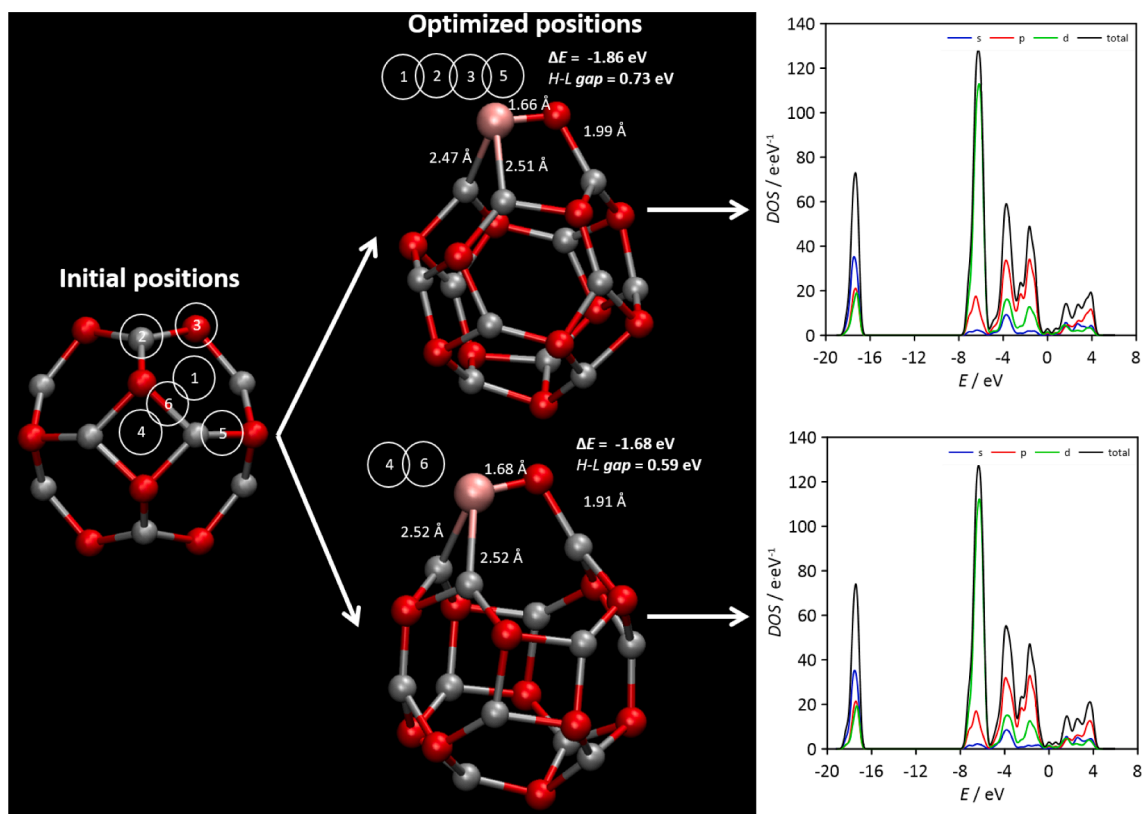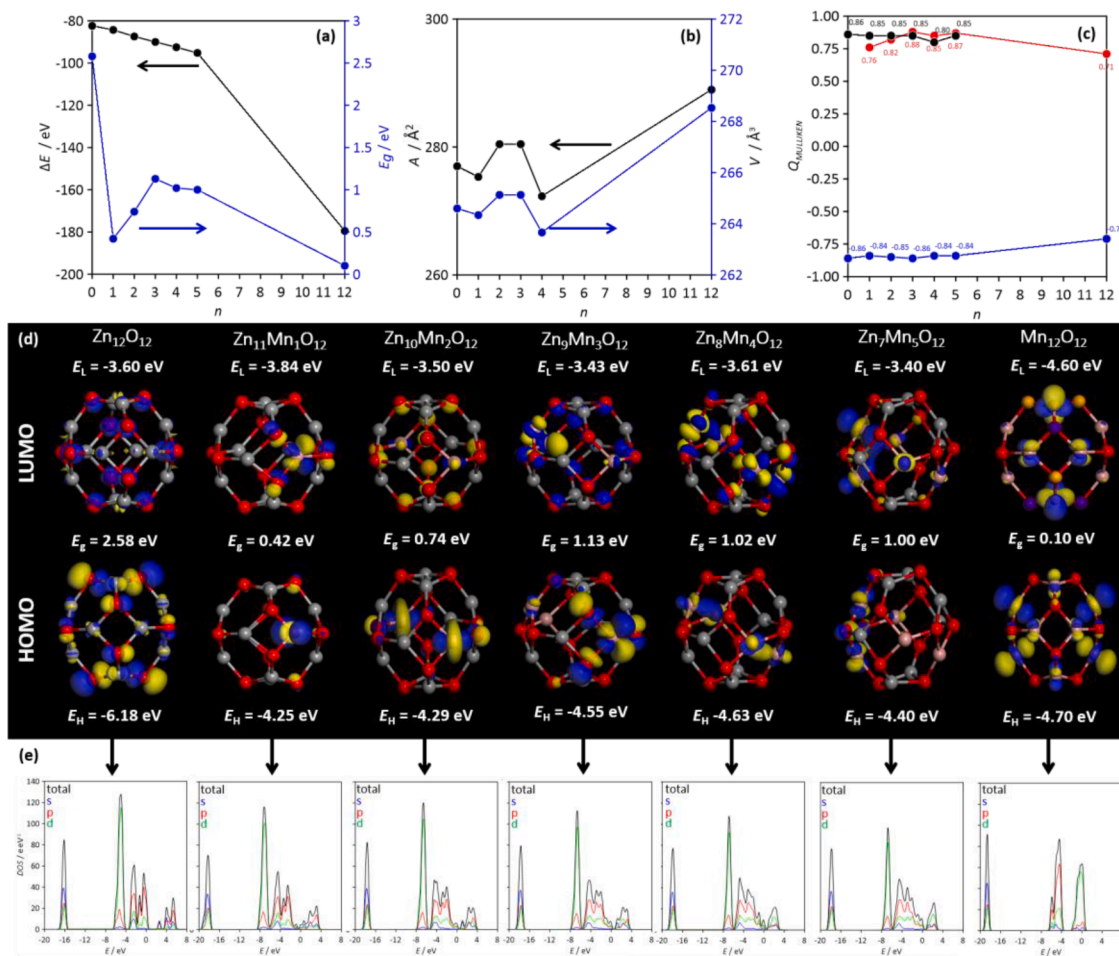

Fig. 7. DFT structures for the adsorption of a single Mn atom on $(ZnO)_{12}$ nanoparticles (Fig. 2a) considering six different adsorption sites. Initially considered positions are indicated as well as optimized positions as well as calculated Density of States. Atom color code: (red) oxygen, (gray) zinc, (pink) manganese.

Fig. 8. DFT calculated properties for ($Zn_{12-n} Mn_n O_{12}$) nanoparticles. Panel (a) shows binding energy, ΔE, and HOMO - LUMO gap, E_g; (b) nanoparticle surface area, A, and volume, V; (c) atomic average Mulliken charges, $Q_{MULLIKEN}$; (e) frontier orbitals; (e) total and partial Density of States, *DOS*. Atom color code: (red) oxygen, (gray) zinc, (pink) manganese.
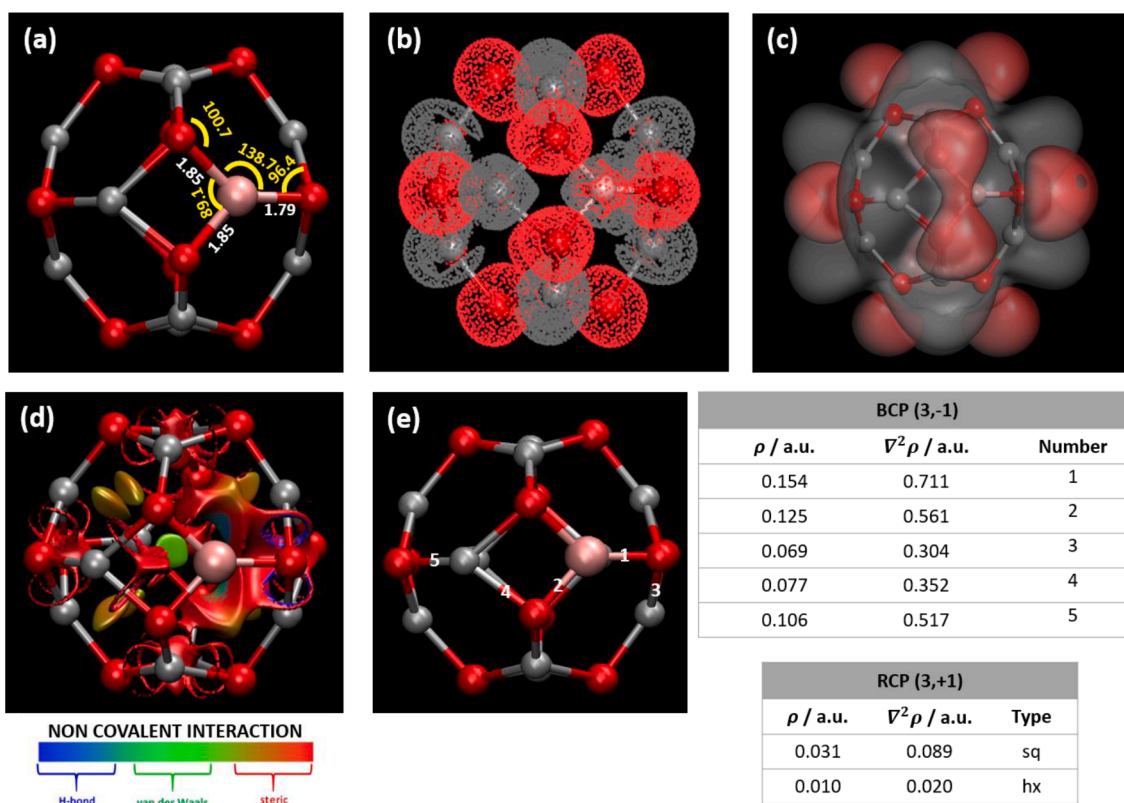
doping and Mn charges being almost equal to those for Zn (with the exception of $n = 1$). This indicate that metal to oxygen charge transfer is not affected by Mn doping. For the case of neat $Mn_{12}O_{12}$ nanoparticles, charges for the metal and oxygen atoms are lower than for $Zn_{12}O_{12}$, Fig. 8c, thus indicating lower trend for charge transfer involving Mn, but this effect is only showed in neat $Mn_{12}O_{12}$ and not present in $Zn_{12}O_{12}$ with Mn doping. The main changes in the $Zn_{12}O_{12}$ nanoparticle properties upon Mn doping appear, as expected, in electronic properties, summarized in Fig. 8d. Doping with Mn atoms leads to a decrease of the HOMO – LUMO gap, with the value for $n = 1$ (0.42 eV) analogous to the gap obtained for a $Zn_{12}MnO_{12}$ nanoparticle with a single Mn atom adsorbed onto the nanoparticle surface (Fig. 7), that is to say, the substitutional doping and adsorptional doping lead to the same changes in electronic properties for the neat nanoparticle. Increasing doping leads to minor changes in the gap, even slightly increasing from 0.42 eV for $n = 1$ to 1.00 eV for $n = 5$, whereas the neat $Mn_{12}O_{12}$ is a conducting material (0.10 eV gap).

The changes in the frontier orbitals upon doping are also reported in Fig. 8d. Results indicate that the main changes are produced in the HOMO orbital, with an energy increase of 1.78 eV on going from neat $Zn_{12}O_{12}$ to the substitutionally doped nanoparticle with $n = 5$ (although this effect is also present with a single atom doping for which HOMO shifts is 1.83 eV). In contrast, the energy of the LUMO orbital only changes 0.24 eV after Mn doping, i.e., the HOMO – LUMO gap closing upon Mn doping is produced by HOMO shifting toward larger energies. Moreover, the location of HOMO orbitals in the structure also changes upon Mn doping: it evolves from $Zn_{12}O_{12}$ case, where HOMO orbitals are

placed on O atoms (mainly composed by 2p orbitals of oxygen), to the $Mn_{12}O_{12}$ case where HOMO orbitals are preferentially placed around Mn atoms and, consistently, with contributions from these metal atoms. Additionally, the contribution of Mn d orbitals to HOMO is confirmed by DOS reported in Fig. 8e, where PDOS for these d orbitals is inferred in the frontier orbitals region.

The changes in Raman and vibrational spectral of nanoparticles upon Mn doping ($n = 1$) may be derived from results in Fig. 3. The main Raman feature corresponding to E_2(high) and assigned to oxygen vibrations, predicted at 407 cm^{-1} for $Zn_{12}O_{12}$ shifts to 438 cm^{-1} for Mn doping with $n = 1$, with a new peak formed at 538 cm^{-1}, with this last peak being typical of Mn doping [75].

Additional characterization of Mn doped ZnO nanoparticles was carried out for doping with $n = 1$ because the large changes in nanoparticle properties are obtained even for single atom doping, Fig. 9. Results in Fig. 9a indicate that Mn – O bonds are roughly 0.1 Å shorter than Zn – O ones (Fig. 4), both, for bonds in squared and hexagonal faces, i.e., stronger bonds can be presumed for pairs involving Mn than for those involving Zn. Additionally, the presence of Mn atoms disrupts squared and hexagonal faces, as the O – Mn – O angles in hexagonal faces are larger than O – Zn – O ones, i.e., hexagonal faces are widened around Mn vertex. These differences in Mn – O and Zn – O covalent bonds are also showed for deformation electron densities reported in Figs. 9b and 3b, where the function around the Mn atoms is disrupted in comparison with Zn sites, with this large deformation being more remarkable in the electrostatic potential reported in Fig. 9c showing the heterogeneity around the Mn site. The disruptive effect of the Mn doping on the

BCP (3,-1)		
ρ / a.u.	$\nabla^2\rho$ / a.u.	Number
0.154	0.711	1
0.125	0.561	2
0.069	0.304	3
0.077	0.352	4
0.106	0.517	5

RCP (3,+1)		
ρ / a.u.	$\nabla^2\rho$ / a.u.	Type
0.031	0.089	sq
0.010	0.020	hx

Fig. 9. DFT calculated properties for $(Zn_{11}MnO_{12})$ nanoparticles. Panel (a) geometrical properties including angles (yellow, deg) and interatomic distances (white, Å); (b) deformation electron density; (c) electrostatic potential, (d) NCI analysis; (e) QTAIM analysis.

topology of electronic distribution is also analysed via NCI and QTAIM approaches. NCI results in Fig. 9d shows that the region around the Mn – O bond is completely different to the one around Zn – O, Fig. 4d, developing a larger steric volume because of the Mn size, with this perturbation even extended to the neighbour Zn – O bonds. Likewise, the NCI feature at the centre of the box corresponding to van der Waals intraparticle interactions is increased upon Mn doping, which would be on the roots of the large stabilization energy reported in Fig. 8 added to the stronger formed Mn – O covalent bonds. The QTAIM analysis shows several relevant results, Fig. 9d, BCPs for Mn – O bonds both for hexagonal and squared faces show larger ρ and $\nabla^2\rho$ values, which confirms stronger Mn – O bonds in comparison with Zn – O ones, i.e., nanoparticle additional stabilization via Mn doping. Likewise, the Mn doping weakens the neighbor Zn – O atoms around the Mn doping site, as inferred from the lowering of ρ and $\nabla^2\rho$, i.e., doping, leading to strong Mn – O bonds and Mn to Zn interactions via weakening of neighbor Zn – O bonds, which is also manifested in the larger perturbation region around Mn doping atom reported in Fig. 9d. Therefore, doping of $(ZnO)_{12}$ nanoparticles with Mn is largely favored and leads to nanoparticles with remarkably different electronic properties, even for single atom doping, and thus doping or adsorption may be considered as effective mechanism for modification of the ZnO – based nanoparticles.

3.5. ZnO nanoparticles behaviour in aqueous solutions

To get insight into ZnO nanoparticles behaviour in aqueous solutions a threefold study has been performed: in a first stage, the interaction of $(ZnO)_{12}$ nanoparticle with explicit water molecule via DFT was considered, in a second one, it was the turn for a specific crystal surface and, in the third step, solvation of $(ZnO)_{12}$ nanoparticles in water was scrutinized via molecular dynamics.

3.5.1. $(ZnO)_{12}$ nanoparticles interaction with water molecules

The behaviour of ZnO nanoparticles in water (i.e. solvation and solubilization) was analysed taking $(ZnO)_{12}$ nanoparticle as a model. As the solvation and solubilization behaviour of ZnO nanoparticles would stand on the nature and strength of nanoparticle–water interactions, in a first stage the adsorption of a single water molecule on nanoparticle surface was studied, Fig. 11. Six different adsorption sites were considered but all of them led to only two possible configurations with large interaction energy, Fig. 11a: (*i*) adsorption on top of nanoparticle oxygen atoms and (*ii*) adsorption on top of Zn atoms, leading to stronger adsorption on Zn sites. NCI analysis of interactions on both sites shows a large blue spot in the region between the water hydrogen atom and nanoparticle oxygen (indicating hydrogen bonding) and also between the water(oxygen) and a Zn atom. In the case of water–nanoparticle interaction through nanoparticle oxygen, the very short interatomic distance as well as the QTAIM results showing the formation of an intermolecular BCP with large ρ and $\nabla^2\rho$ indicate the development of intermolecular hydrogen bonding. Indeed, according to Popelier and Koch [76] hydrogen bonds are characterized by BCPs with ρ and $\nabla^2\rho$ in the 0.002–0.035 a.u and 0.024–0.139 a.u. ranges, respectively, with larger values corresponding to stronger interactions. The interaction reported in Fig. 11a would be even above the hydrogen bonding threshold, showing a very strong interaction with partial proton transfer from water to the nanoparticle. For the interaction with water through the Zn sites, the developed BCP with the reported ρ and $\nabla^2\rho$ as well as the short Zn to water (oxygen) distance also indicate very strong interaction. Although the Zn – O(water) distance, 2.13 Å, is larger than the Zn – O(nanoparticle) bond, 1.9 to 2.0 Å, Fig. 4a, it may be considered as a weaker Zn – O covalent bond. Regarding the changes in the nanoparticle properties via water molecule adsorption, NCI results in Fig. 11a indicate negligible changes with regard to clean nanoparticle, Fig. 4d. Changes on nanoparticle electronic properties are quite subtle: the adsorption of water molecule leads to minor modifications of the HOMO

– LUMO gap, evolving from 2.58 eV (non-Hubbard corrected for clean nanoparticle) to 2.18 eV upon hydrogen bonding on oxygen atoms, or to 2.53 eV for interaction through Zn sites. Changes in DOS are also negligible upon water adsorption (Figs. 5 and 11b,c). Adjustments in water molecule upon adsorption on the nanoparticle surface are as follows: oxygen–hydrogen intramolecular bond distance evolves from 0.96 to 0.98 Å (to 1.01 Å for the hydrogen atom involved in hydrogen bonding with the nanoparticle) and the O–H–O dihedral angle varies from 109.5 to 105.1°. In conclusion, almost negligible changes are induced on water molecules even after the reported strong intermolecular interaction, maintaining their integrity on the nanoparticle surface.

A second mechanism of water–nanoparticle interaction was considered through the formation of endohedral water–ZnO nanoparticle complexes via the encaging of a water molecule into the cavity. Results for the optimized structure of the endohedral complex are reported in Fig. 12b and compared with the clean nanoparticle, Fig. 12a. The water encaging results in a perturbation of the nanoparticle structure which is quantified as a volume expansion of 2.46 Å^3 and a increase of accessible area (9.63 Å^2) also accompanied by a minor elongation of Zn-O nanoparticle bonds, Fig. 12a. Likewise, the endohedral complex has a lower HOMO-LUMO band gap, although the semiconductor character is maintained, with changes in the DOS only produced by orbitals above the LUMO one, Fig. 12b. The possible penetration of water molecules inside the empty hollow nanoparticle trough squared faces is sterically hindered but it is not through hexagonal ones. In spite of this possibility, results in Fig. 12c and d indicate a large barrier (11 eV) through the hexagonal face, which almost discards the penetration mechanism. Endohedral complexes could be formed mostly via encaging of water molecules during the formation of (ZnO)$_{12}$ nanoparticles and this is the reason to define E_{endo} in the way shown in Eq. (7).

3.5.2. ZnO {1 0 0} surface exposure to water

Small nanoparticles with diameters lower than 3 nm, Fig. 2, have been considered in previous sections. The analysis of larger nanoparticles and the development of a more realistic model of their exposed surfaces, which will control the majority of their most relevant properties, has been developed following a two steps procedure: (*i*) the stability of ZnO surfaces has been quantified in terms of surface energy and (*ii*) a nanoparticle model using Wulff construction method based on obtained $E_{surface}$ as defined in Eq. (8).

The unit cell for ZnO bulk crystal wurtzite structure was considered as starting point and it was optimized as indicated in Section 2.2 leading to unit cell parameters in agreement with literature. To check the effects of Mn doping on crystal structure a 10 % atom percentage doping was considered and the simulated crystal lead also to a wurtzite like structure with $a = 3.30$ Å and $c = 5.36$ Å, which shows a unit cell expansion of

5.3 % in volume upon doping but with negligible structural changes. The optimized unit cell was cleaved along relevant Miller indices and the corresponding $E_{surface}$ were calculated, Fig. 10a. The reported $E_{surface}$, in the range from 0.80 to 1.09 J m^{-2}, show low values for the most relevant Miller indices, thus indicating high stability in all the cases. As the larger nanoparticles may have surfaces with a large variety of Miller indices and, consequently, different physicochemical properties, previous $E_{surface}$ results have been used as parameters to propose a model of a representative cubic nanoparticle. The realistic model of a large nanoparticle illustrated in Fig. 10b shows large exposed surfaces with {1 0 2} indices in all the faces, whereas regions for {0 0 2} indices correspond to surfaces formed at the centre of the faces and minor surfaces at the vertices have {1 1 2} indices.

The effect of the type of surface exposed to water environment was studied by considering low index – low surface energy {1 0 0} surface, Fig. 10a, as obtained from bulk crystal surface and considering AIMD simulations, Fig. 13. In this surface both, Zn and O atoms, are exposed to the surface, so interaction with water via the two mechanisms inferred from Fig. 11 could be analyzed beyond the initially considered single water molecule approach. Results in Fig. 13a show the formation of up to four adsorbed water layers on the considered surface, indicating high affinity between water molecules and ZnO surface. The Radial Distribution Functions (RDFs) reported in Fig. 13b for the interaction between O atoms in water and O / Zn atoms in the surface correspond to strong interactions and to hydrogen bonding for the case of O(water) – O(ZnO), in agreement with DFT results in Fig. 11a. This confirms the two adsorption mechanisms via O and Zn atoms on the surface for the water liquid phase. The water adsorption on the considered surface is also accompanied by water – water hydrogen bonding. This is illustrated in Fig. 13b, where O(water) – O(water) RDF shows almost negligible changes for the molecules in the adsorbed layers when compared with bulk liquid phase. Nevertheless, the water adsorption leads to a decrease of water molecules mobility as indicated by the reduction of molecular self – diffusion and the changes in Velocity Autocorrelation Function (VACF), Fig. 13c, confirming the strong water to surface affinity.

3.5.3. (ZnO)$_{12}$ nanoparticles behaviour in aqueous solutions: solvation and solubilization

Further analysis was carried out considering explicit, in contrast with surfaces in Fig. 13, (ZnO)$_{12}$ nanoparticles in water using a double approach: AIMD and classical MD simulations, Fig. 14. First, results for explicit nanoparticles are in fair agreement between both theoretical approaches, Fig. 11, and also with those results considering only exposed surfaces, Fig. 13. So, it can be concluded that the behavior of nanoparticles in aqueous solution can be inferred from simple surface models as those shown in Fig. 13. But also, that so large nanoparticle
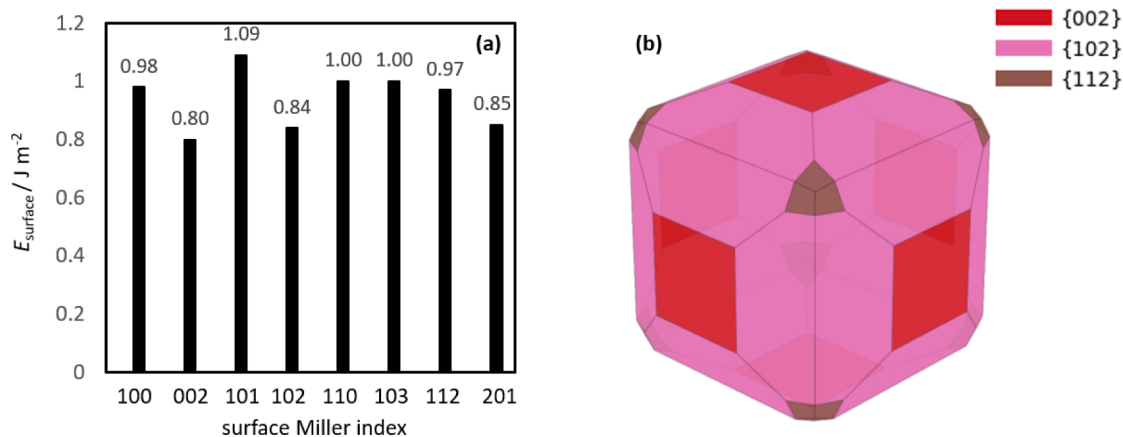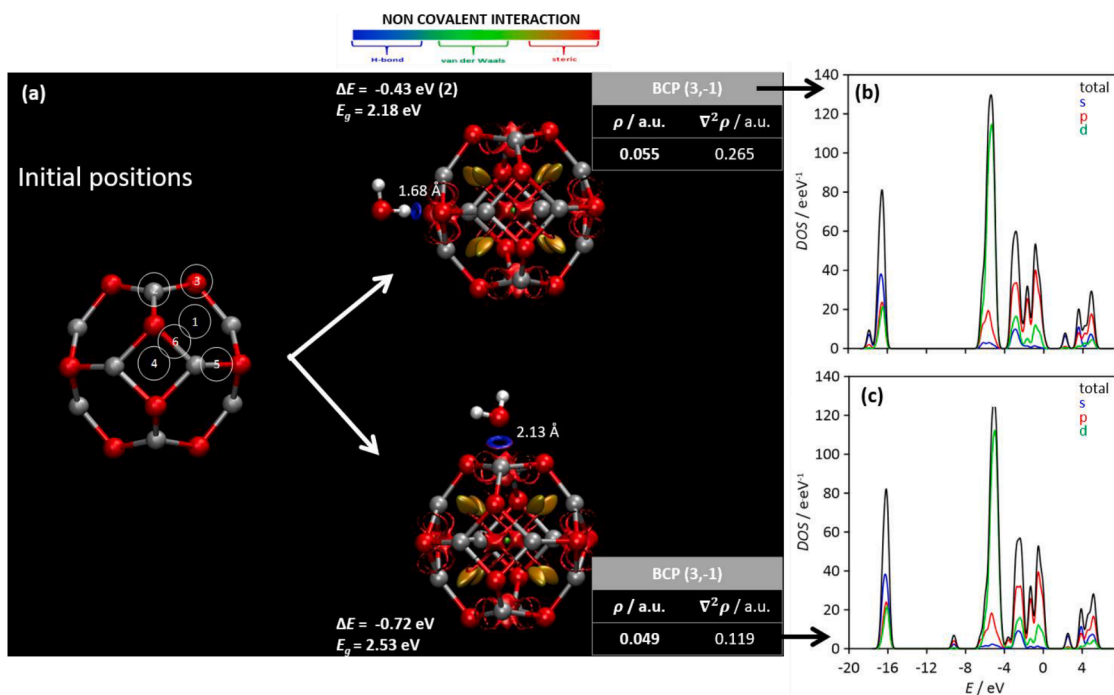

Fig. 10. (a) DFT-TB calculated surface energy, $E_{surface}$, for surfaces of ZnO for different Miller indices and (b) Wulff construction for model cubic nanoparticle calculated from $E_{surface}$ values.

Fig. 11. DFT calculated structures and properties for the adsorption of a single water molecule on the surface of $(ZnO)_{12}$ nanoparticle (Fig. 2a). Reported properties consider water – nanoparticle binding energy, HOMO – LUMO gap, *H-L gap*, NCI and QTAIM analysis as well as Density of States. Atom color code: (red) oxygen, (gray) zinc.

models as those built after Wulff method using surface properties, Fig. 10, would be realistic representations of ZnO nanoparticles properties. Therefore, as the results for $(ZnO)_{12}$ nanoparticles simulations are in fair agreement with larger model particles and surfaces, to model the possible aggregation of multiple nanoparticles in water, the $(ZnO)_{12}$ nanoparticle was chosen.

The results in Figs. 13 and 14 could be summarized as: (*i*) strong water–nanoparticle interaction and thus efficient solvation, (*ii*) water molecules interaction with nanoparticles both via Zn and (hydrogen bonding) O sites, and (*iii*) reduction of water molecular mobility but with water - water hydrogen bonding being preserved upon adsorption. The strong water-nanoparticle interaction is depicted as the high intensity peaks reported in the RDFs between the Zn and O atoms of the nanoparticles and both the H and the O atoms of the water molecules. This high intensity peaks indicate a strong interaction of these two entities, leading to the solvation of the nanoparticle. The distances reported in the RDFs for the interactions of H and O atoms from water and O atoms from ZnO nanoparticle (Hw-OZn 1.50 Å and Ow-OZn 2.75 Å) are consistent with the formation of hydrogen bonds between water and nanoparticles. The reduction of water molecular mobility is caused by formation of adsorbed layers on the exposed surface. The adsorption of water molecules, and therefore, their reduced molecular mobility enhances the interaction between the water molecules, as the first RDF peak between oxygen atoms is more intense for the adsorbed molecules than for the molecules in the bulk.

The water–nanoparticle hydrogen bonding is confirmed through results in Fig. 15, with analogous results for AIMD and classical MD simulations as well as minor changes in water self-association through hydrogen bonding upon surface adsorption. This efficient $(ZnO)_{12}$ nanoparticle solvation effect in water solutions would hinder nanoparticles self-aggregation allowing their solubilization in aqueous solutions.

In spite of the large stabilization of ZnO nanoparticles via efficient solvation in aqueous solutions previously shown, the possible release of Zn atoms in water was calculated using DFT-TB for the analysis of Zn removal barriers from different surfaces. Results in Fig. 16 from main

exposed surfaces (large nanoparticle model in Fig. 10b) indicate energy barriers in the 7.5–9.0 eV range. Thus, very slow Zn solubilization, i.e., cation release in aqueous solution from nanoparticles is deduced, suggesting long-time stable nanoparticles. These high Zn removal energy barriers are in agreement with experimental solubilization studies for nanoparticles with sizes in the 40–70 nm range. Their solubilization rates are roughly 8 μg L^{-1} h^{-1}, being even slower for smaller nanoparticles. These moderate rates lead to dissolved Zn concentration as low as 2.2 mg L^{-1} (starting from 100 mg L^{-1} of nanoparticle, i.e. 2.2 % solubilization) after 34 days. Solubilization is almost negligible when water phase conditions are modified, using hard water, which gives rise to ZnO nanoparticles persisting in the (aqueous) environment [77]. It can be concluded that the nanoscopic reason for this persistence are the large solubilization barriers reported in Fig. 16.

3.6. Biological behaviour of nanoparticles

The possible biological effects of ZnO nanoparticles, specifically the toxicological ones in humans, was studied in silico by considering a tow-fold approach: (*i*) nanoparticle interaction with model cell membranes and (*ii*) interaction (docking) of nanoparticle with human proteins. The $(ZnO)_{12}$ nanoparticle was considered as a model since it is well known that possible toxicological effects are exacerbated with decreasing nanoparticle size.

In the first approach, plasma cell membranes composed of DPPC lipids were considered. The strength of the lipid – nanoparticle interaction was initially explored with DFT-TB studying interactions with different exposed surfaces. Results in Fig. 17a indicate very effective lipid – surface interactions, leading to the adsorption of lipid molecules on the surfaces with large interaction energies (0.9–1.2 eV range). This lipid–surface adsorption should lead to a competing effect between lipid – lipid interactions and it may favour nanoparticle penetration into DPPC lipid bilayers. Nevertheless, the lipid–surface (nanoparticle) interaction energy is lower than the lipid-lipid one, with a calculated value of 2.1 eV per lipid pair. A more realistic model was proposed and the interaction of $(ZnO)_{12}$ nanoparticle with DPPC molecule was
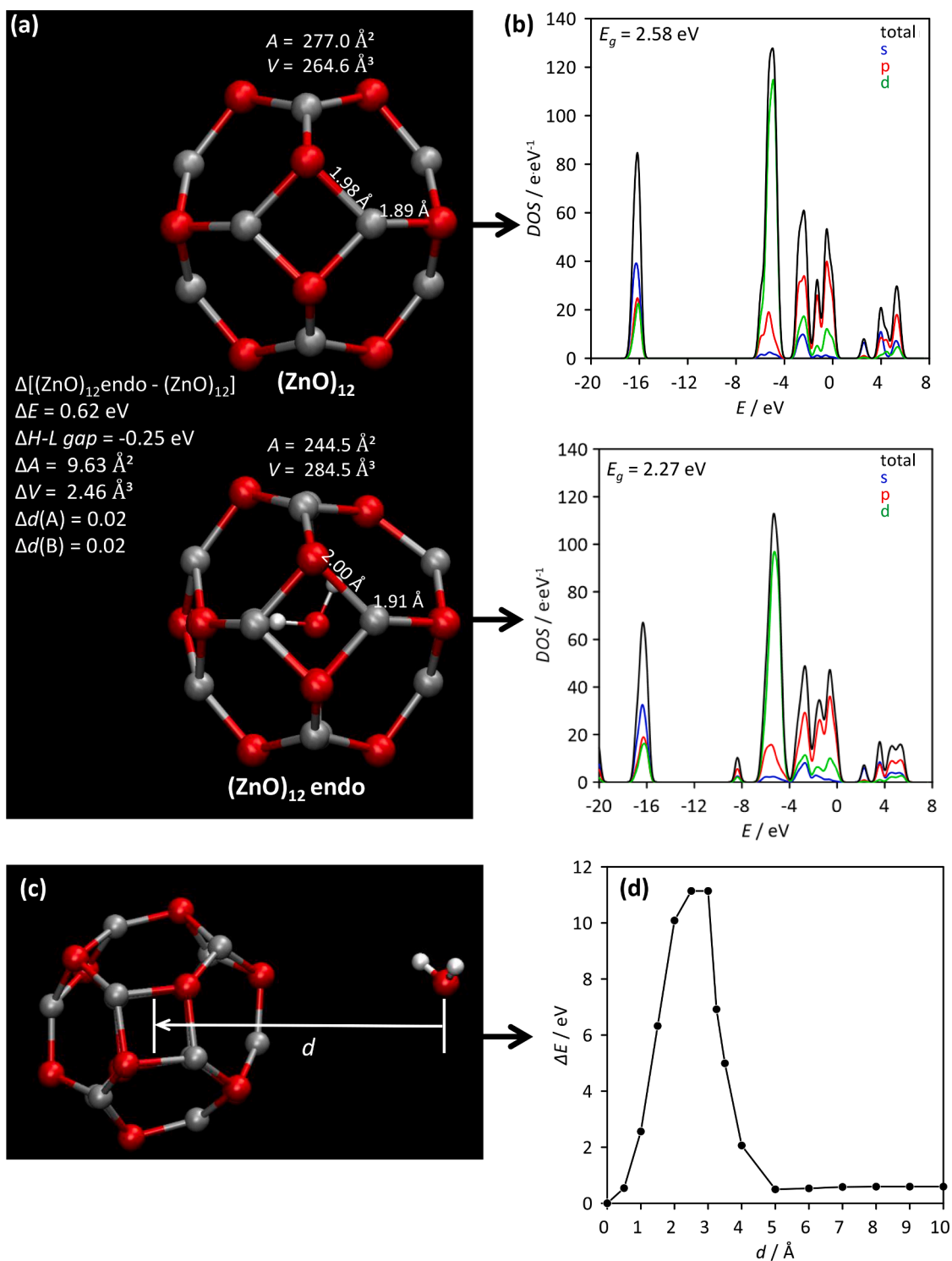
Fig. 12. (a,b) DFT calculated properties of endohedral water confined inside (ZnO)$_{12}$ nanoparticle reporting HOMO - LUMO gap, E_g, nanoparticle surface area, A, and volume, V, and total and partial Density of States, *DOS*. The differences between the (ZnO)$_{12}$ clean nanoparticle and the geometry of the nanoparticle containing the water molecule are calculated in terms of the properties presented. Panels (c,d) show the penetration barrier for water molecules inside the nanoparticle cavity reporting the water – nanoparticle binding energy, ΔE.

calculated taking into account the different possible interaction sites, Fig. 17b. The interaction energies for the nanoparticle–lipid are in the range of those for surface–lipid, and thus they confirm efficient nanoparticle interaction with the lipid. Nevertheless, there is a large heterogeneity in the values reported in Fig. 17b, with remarkable stronger interaction with phosphate and glycerol groups and weaker interactions with choline head group and non-polar alkyl chains. The values of

interactions with choline and alkyl groups are remarkably lower than those for lipid – lipid interactions. So, the disruption of lipid bilayers by interaction with nanoparticle would be effective only once the nanoparticle penetrates into the head groups and we may expect that lipid – lipid interactions (mainly through alkyl – alkyl interactions) would not be disrupted by nanoparticles in view of the weaker character of interaction with nanoparticles.
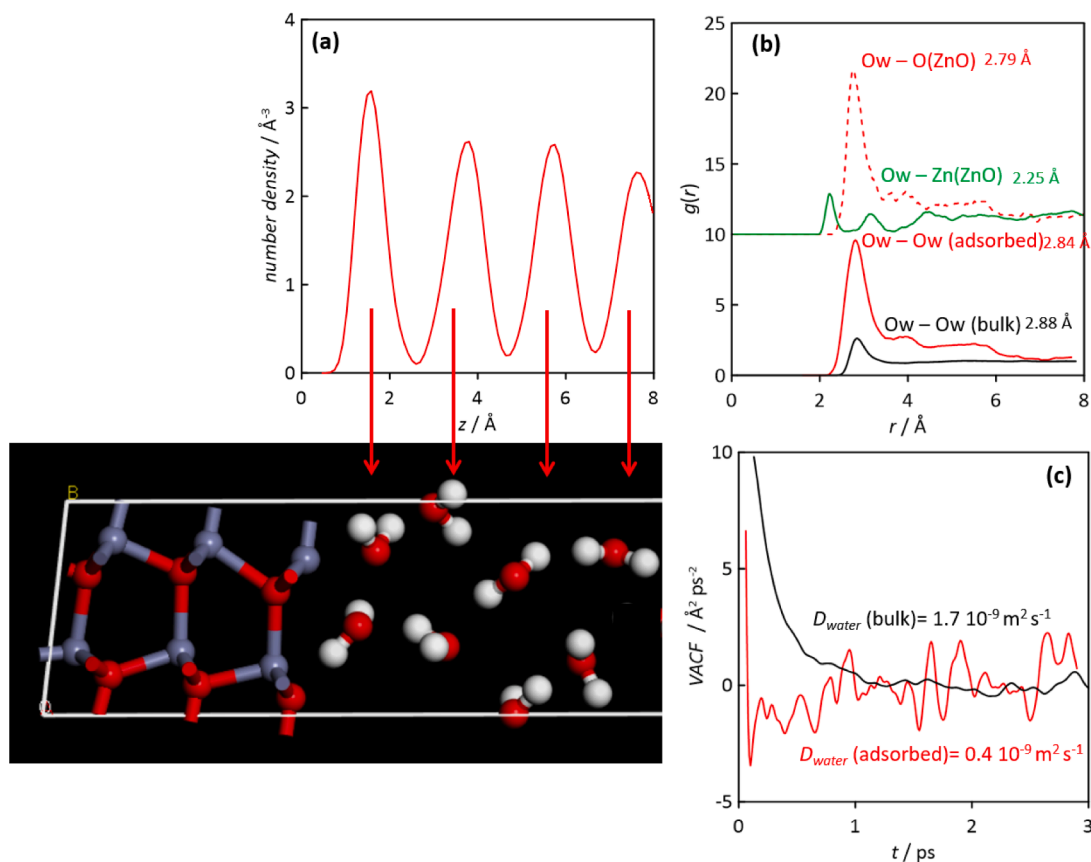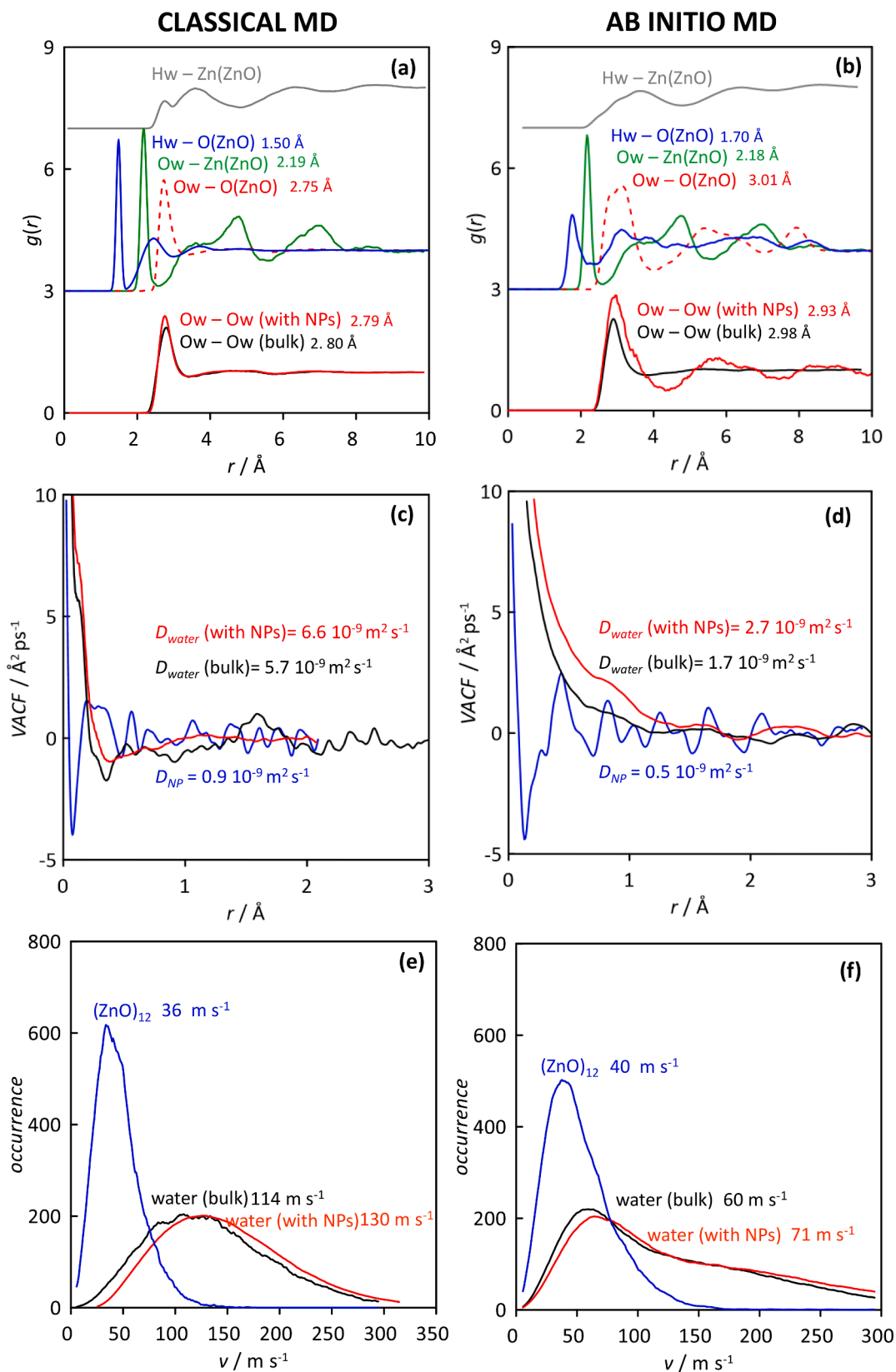
Fig. 13. AIMD (DFT-TB) (303 K and 1 bar) results for water liquid layer on top on (ZnO) {1 0 0} surface showing: (a) number density profile of water center-of-mass, (b) site – site Radial Distribution Functions for relevant atoms, $g(r)$, and (c) center-of-mass Velocity Autocorrelation Functions, VACF. Result for water molecules are reported for water molecules in presence of $(ZnO)_{12}$ {1 0 0} (labelled as adsorbed) and for neat water phase (i.e. liquid water in absence of the surface, labelled as bulk).

The interaction of model $(ZnO)_{12}$ nanoparticles with plasma cell membranes was proposed as a possible Molecular Initiating Event (MIE) into an Adverse Outcome Pathway (AOP) concept for possible toxicity effects [78,79]. The mechanism of interaction was studied using coarse grained MD simulations. A DPPC lipid bilayer was built and put in contact with an aqueous phase containing nanoparticles at four different concentrations: 0, 1.5, 4.5 and 8.5 wt%. A new force field parameterization, on the Martini CG forcefield framework, was carried out to simulate nanoparticle – lipid interactions. As ZnO nanoparticles were described as composed of ZnO beads, i.e. $(ZnO)_{12}$ nanoparticle formed by twelve ZnO beads, the interaction of this type of bead with molecular moieties resembling those parts of DPPC lipid molecule – choline, phosphate, glycerol and alkyl groups – were calculated using DFT-TB from which CG forcefield parameters were obtained and used for CGMD simulations. The ZnO bead interaction curves with different lipid molecular moieties are reported in Fig. 18 in agreement with results in Fig. 17, showing stronger interactions with phosphate and glycerol moieties as well as strong interactions with water molecules as indicated in previous sections for the nanoparticle behaviour in aqueous solutions.

Results of the CGMD simulations for the systems are reported in Fig. 19a and their remaining panels, where several properties of the lipid bilayer are considered to infer the possible disruptive or perturbative effect of the nanoparticles in aqueous solution. The bilayer in contact with neat water phase (0 wt% for nanoparticles) was taken as a reference. As a first key result, $(ZnO)_{12}$ nanoparticles considered in the 0 to 8.5 wt% range do not penetrate into the DPPC lipid bilayer for the CGMD simulations during a time interval of 1000 ns. As nanoparticles wander around the bilayer surface it can be concluded that they are not physically bonded moving in and out from the aqueous solution liquid

layer in contact with the surface. Therefore, according to the simulation ZnO nanoparticles would not cross cell membranes, remaining in the outer (cell) regions. Nevertheless, the possible perturbative effects were initially quantified by determining the bilayer distribution as well as the width and surface area per lipid molecule, Fig. 19b and c. Density profiles reported in Fig. 19b suffer very minor changes for lipid bilayer upon increase of nanoparticle concentration. The calculated bilayer width, Fig. 19c, evolves from 3.80 nm for 0 wt% concentration (bilayer in contact with neat water, in agreement with literature values reporting widths in the 3.6 to 3.8 nm range [59,80]) to 3.99 nm for 8.5 wt% concentration of ZnO nanoparticles. Likewise, the area per lipid decreases from 0.70 nm^2 for bilayer in contact with clean water (slightly larger than literature values in the 0.63 to 0.67 nm^2 [59,75]) to 0.68 nm^2 when the bilayer is in contact with 8.5 wt% nanoparticle concentration. Both properties evolve in a close to linear way ($R^2 = 0.98$) with increasing nanoparticle content. Therefore, exposure to nanoparticles is accompanied by a minor expansion along the direction perpendicular to the surface along with a contraction in the bilayer plane, which leads to a decrease in the interdigitation of lipid alkyl chains from 0.52 (neat water) to 0.48 nm (8.5 wt%). Nevertheless, the induced changes by the presence of nanoparticles in the aqueous solution in contact with the bilayer are very minor and the integrity of the bilayer is preserved for the studied nanoparticle concentration range. This negligible effect induced by the nanoparticles are compatible with results in Fig. 19b which show how ZnO nanoparticles remain on top of the surface of one of the bilayer leaflets (outer region of the cell) with increasing nanoparticle concentration. The presence of the nanoparticles on top of the bilayer leads to inconsequential changes in the arrangements of lipids as probed by the reported internal angles of the lipids (Fig. 19d) and the

CLASSICAL MD

AB INITIO MD

Fig. 14. Properties for $(ZnO)_{12}$ nanoparticles (NP) in liquid water as obtained from classical Molecular Dynamics (MD) and AIMD (DFT-TB) simulations at 303 K and 1 bar. Results show: (a,b) site – site Radial Distribution Functions for relevant atoms, $g(r)$, (c,d) center-of-mass Velocity Autocorrelation Functions, VACF, and (e,f) center-of-mass Velocity Distribution Functions. Result for water molecules are reported for water molecules in presence of $(ZnO)_{12}$ nanoparticles (labelled as adsorbed) and for neat water phase (i.e. liquid water in absence of the nanoparticles, labelled as bulk).
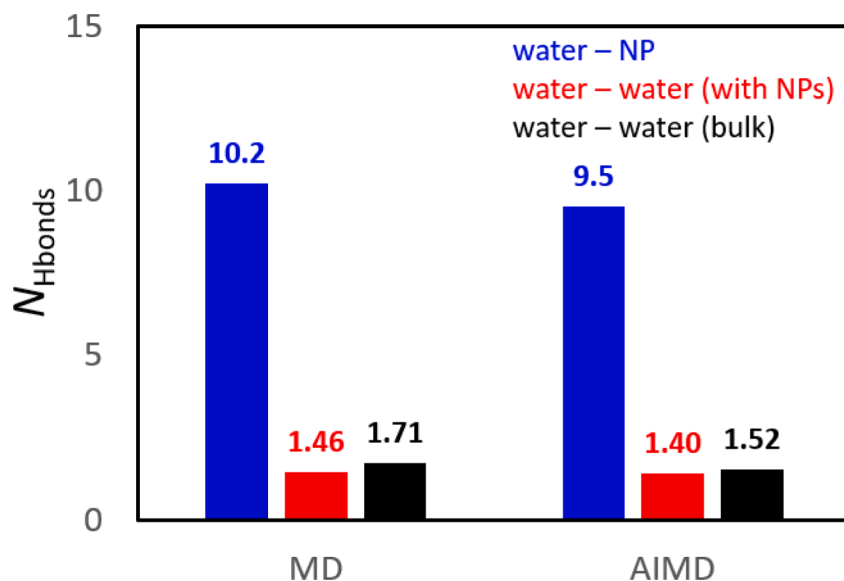
Fig. 15. Average number of Hydrogen Bonds, N_{Hbonds}, for the reported molecular pairs for $(ZnO)_{12}$ nanoparticles (NP) in liquid water as obtained from classical Molecular Dynamics (MD) and AIMD (DFT-TB) simulations at 303 K and 1 bar. Results for water molecules are reported for water molecules in presence of $(ZnO)_{12}$ nanoparticles (labelled as adsorbed) and for neat water phase (i.e. liquid water in absence of the nanoparticles, labelled as bulk). Values are reported per $(ZnO)_{12}$ nanoparticle for water – NP and per water molecule for water – water.
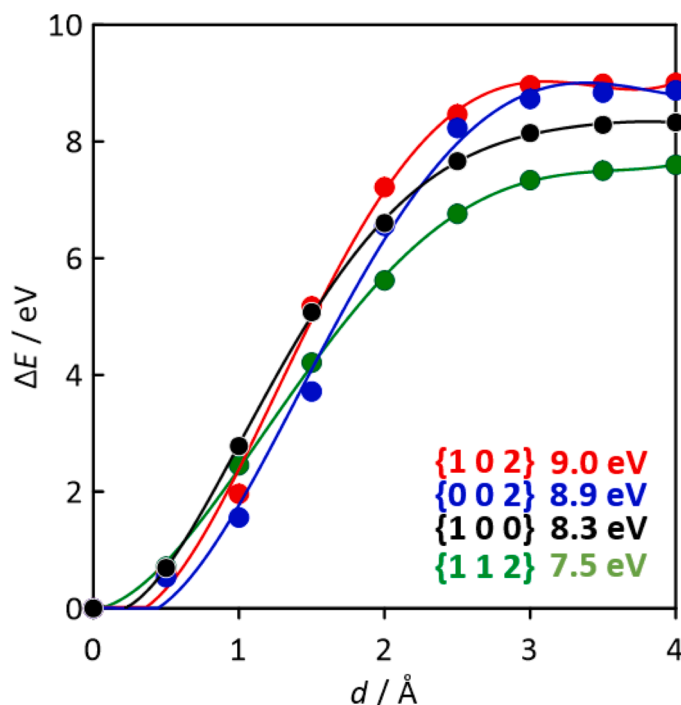

Fig. 16. DTF-TB calculated energy barriers, ΔE, for the removal of Zn atoms from ZnO surfaces, with indicated Miller indices with distance to the surface, d.

alkyl chain length (Fig. 19d).

Despite these slight structural changes in the lipid bilayer, the dynamic properties of the lipid suffer more remarkable changes upon exposure to the ZnO nanoparticles. The in-plane self-diffusion coefficients reported in Fig. 19f increase in a linear way ($R^2 = 0.99$) 0.61 10^{-11} to 2.06 10^{-11} m^2 s^{-1} (i.e., 3.4 times larger molecular diffusion rates) on going from neat to 8.5 wt% solutions. Likewise, as shown in Fig. 19g, time constants for the Rotational Correlation Functions of head and tail lipid vectors, faster for head than for tail, also increase with increasing nanoparticle concentration. To sum up, the CGMD results indicate almost negligible changes in DPPC bilayer structure in contact

with ZnO nanoparticle solution, even for high concentration (8.5 wt%). The only noticeable effect being a slight increase of bilayer thickness but accompanied by an increase in lipid mobility produced by the presence of nanoparticles in the vicinity of the surface region of the upper leaflet. Therefore, it is to be expected from the point of view of interactions between nanoparticles and cell membranes, that ZnO nanoparticles, whose results in previous sections confirmed their integrity in aqueous solutions, have minor (toxicological) biological effects for reasonable exposure scenarios (cells in contact with nanoparticle solutions with concentrations lower than 8.5 wt%).

For the second approach of in silico (toxicological) biological effects,
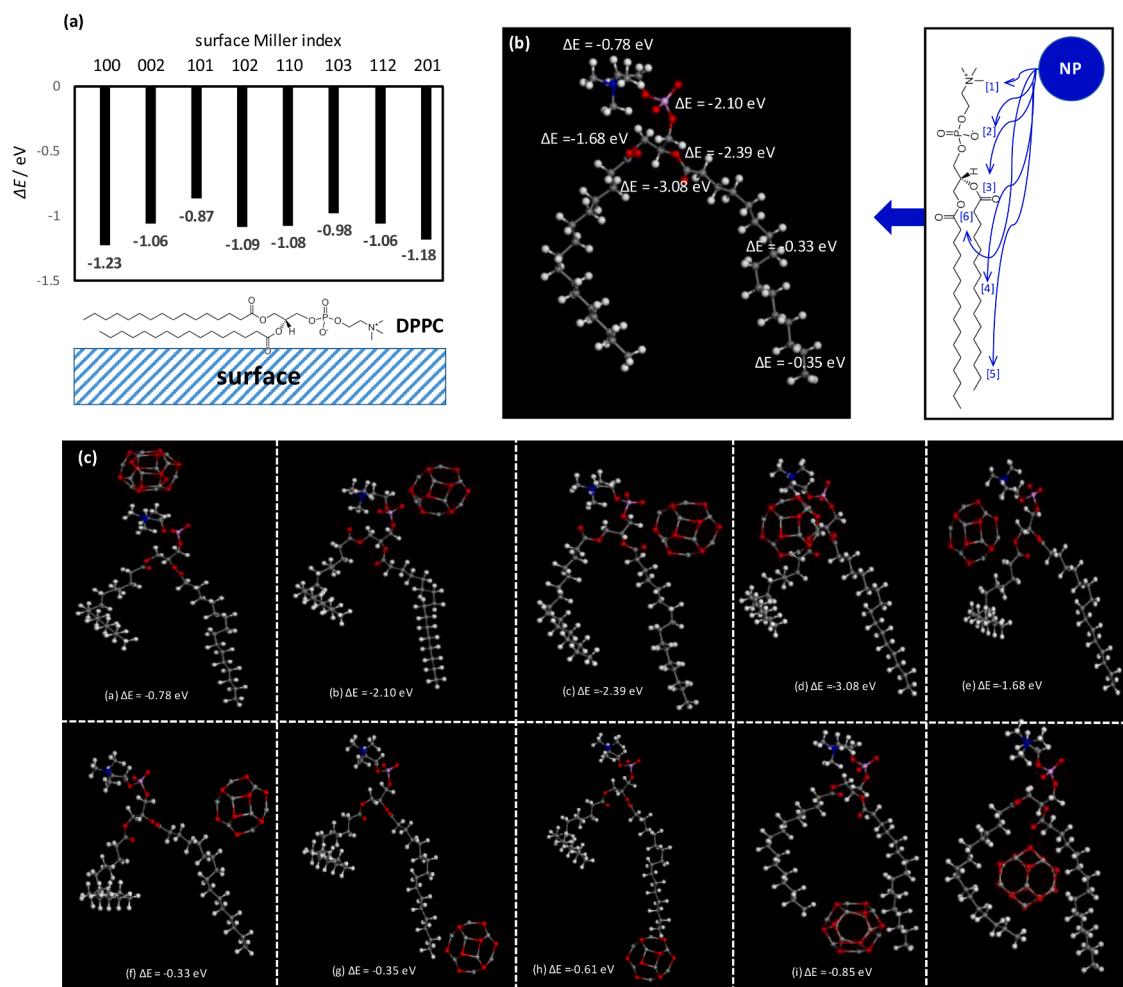
Fig. 17. DFT calculated interaction energy, ΔE, of DPPC molecule with (a) ZnO surfaces as indicated by the corresponding Miller indices and (b,c) with $(ZnO)_{12}$ nanoparticle for the corresponding sites in DPPC molecule.

docking studies of $(ZnO)_{12}$ nanoparticles on a set of selected human proteins of different families (functions) were carried out. The proteins were selected considering several possible targets for the nanoparticles. The affinity of the nanoparticles for the active sites of each protein was quantified in terms of binding energies and discussed as an additional indicator of possible toxicological effects.

Further information about the interaction of the considered nanoparticles with biological targets was obtained from docking studies of neat $(ZnO)_{12}$ nanoparticles, as well as for Mn-dopped ones ($Zn_{11}MnO_{12}$ and $Zn_7Mn_5O_{12}$ were taken as representatives). $(MnO)_{12}$ was selected as well. In this study 102 human proteins belonging to 25 different families were chosen (Table S1, Supplementary Information). Different nanoparticle-protein configurations were ordered according to their binding energies. The resulting 9 first configurations for each nanoparticle – protein interaction was considered and their binding energies were averaged leading to the value of $E_{binding}$ reported in Table S1, Supplementary Information. Results were summarized in Fig. 20a. First, $E_{binding}$ ranges from −9.7 to −5.0 kcal mol^{-1}, which correspond to moderate nanoparticle–protein interaction, in other words the effect of protein disruption through efficient coupling of nanoparticle(s) into the protein active sites is rather weak. Second, results in Fig. 20a do not show remarkable difference between the type of nanoparticles for a fixed type of protein, in fact, the standard deviation considering the effect of nanoparticle is 0.2 kcal mol^{-1}, which points to analogous effect (s) for the four considered nanoparticles.

Fig. 20b depicts the frequency distribution of each nanoparticle exhibiting the highest binding energy to a fixed protein. The results

indicates that the presence of Mn atoms in the nanoparticle promotes a stronger interaction with the protein, implying that Mn-doped nanoparticles may exhibit a potentially more toxic behaviour. However, it is important to note that the energy values for the Mn-doped nanoparticles are closely comparable to those of the other nanoparticles considered as mention before.

Third, there is not a specific effect on the type of protein, with the nanoparticles showing similar $E_{binding}$ ranges for all the protein families, i.e., all the nanoparticles interact with the similar strength with the considered 25 families of proteins without preferred interaction. This effect, show that the considered nanoparticles may interact moderately with the large diversity of considered proteins. This should lead to some caution as a diversity of biological effects could be produced although the $E_{binding}$ ranges indicate that in all the cases these effects would be moderate leading to minor biological disruption. Additionally, the possibility of having some kind of effect considering the nanoparticle type was analysed through classification using coarse gaussian Support Vector Machine (SVM) learning (the best inferred option). Results in Fig. 20b show poor classification, with True Positive Rates (TPR) in the 18–22 % range, i.e., there is not a well-defined nanoparticle effect on the inferred $E_{binding}$, which may be justified considering the moderate strength of the interactions and the similar effects for all the nanoparticles in all the protein families, i.e. moderate although varied (toxicological) biological effect.
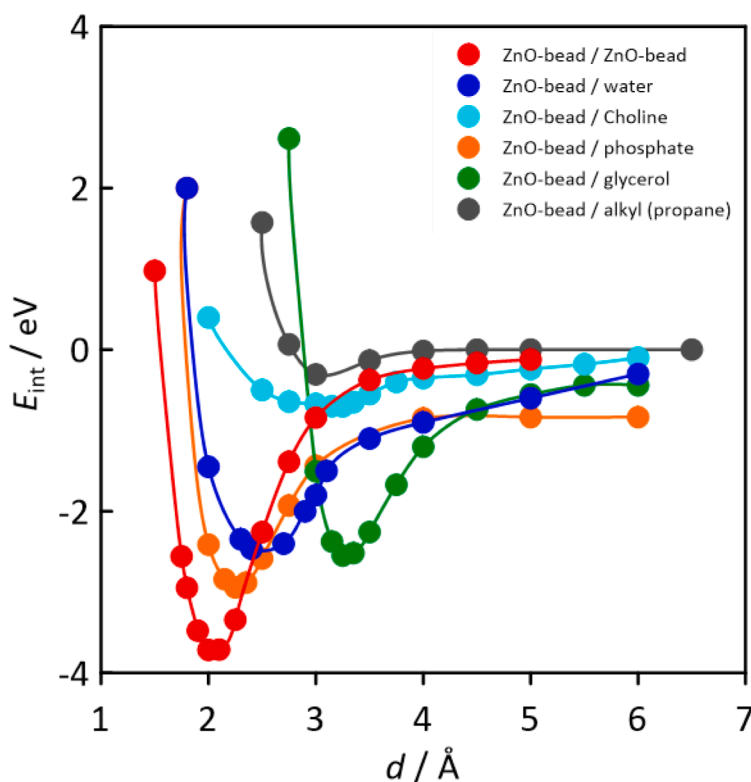
Fig. 18. Results for the interaction between ZnO and the indicated molecular moieties. Symbols indicate results as obtained from DFT-TB for (ZnO) – molecules interactions and lines show results from CG-Martini for the interaction of (ZnO) – beads and the beads corresponding for the reported molecules with interaction parameters estimated from DFT-TB results.

4. Conclusions

The behaviour of Zinc Oxide nanoparticles, pure and Manganese doped, was studied using a multiscale modelling simulation. The properties of nanoparticles were inferred from first principles simulations in terms of particle size and shape. The binding energy has a linear response to the increase of (ZnO) units and the HOMO-LUMO gap decreases as the NPs size increases. The mechanism of nanoparticle growing via aggregation from small nanoparticle seeds is confirmed as the formation energy for larger NPs obtained are in good agreement with the interaction energy reported for hollow NPs. Efficient adsorption (ΔE = -1.7 and ΔE = -1.9 eV) and doping (ΔE = -84.3 eV for $Zn_{11}MnO_{12}$ to ΔE = -95.2 eV for $Zn_7Mn_5O_{12}$) with Mn atoms were inferred leading to a large modification of nanoparticle electronic properties. The behaviour of nanoparticles in aqueous solutions was studied showing efficient solvation based on the adsorption energy for water molecules reported with DFT (ΔE = -0.4 and ΔE = -0.7 eV) and the adsorption of water molecules up to four layers on the {1 0 0} ZnO surface. The hydrogen bond network developed between H and O atoms from water molecules and O atoms from ZnO NP supports the efficient solvation conclusion. The very minor solubilization of ZnO NP, with energy barriers raging from 7.5 to 9.0 eV for the removal of Zn atom from different ZnO surfaces, leads to stable nanoparticles in aqueous solutions. The in-silico studies for the interaction with model cell membranes and human proteins showed minor disruption of these biological structures. The ZnO NP do not cross the bilayer as the preferred interaction site for the NP are O atoms located on the head groups of the DPPC lipids (ΔE = -3.1 eV) whilst the interaction with the lipid hydrocarbon chains is quite weaker (ΔE = -0.3 eV). The affinity energies for the ZnO and Mn doped NPs range from -5.0 to -9.8 kcal/mol for all the human proteins considered. These results point to stable nanoparticles in aqueous solutions in contact with cells but with low toxicological effects for reasonable concentration of nanoparticles which may be produced after human and environmental exposure to products containing these nanomaterials.

Supplementary information

Table S1 (nanoparticle – proteins docking results).

CRediT authorship contribution statement

Nuria Aguilar: Conceptualization, Data curation, Formal analysis, Investigation, Methodology, Validation, Visualization, Writing – original draft, Writing – review & editing. **Sara Rozas:** Data curation, Formal analysis, Investigation. **Elisabeth Escamilla:** Data curation, Formal analysis, Investigation. **Carlos Rumbo:** Conceptualization, Data curation, Funding acquisition, Investigation, Supervision, Writing – original draft, Writing – review & editing. **Sonia Martel:** Conceptualization, Data curation, Formal analysis, Funding acquisition, Investigation, Project administration, Writing – original draft, Writing – review & editing. **Rocío Barros:** . **Pedro Angel Marcos:** Conceptualization, Data curation, Formal analysis, Investigation, Methodology, Supervision, Writing – original draft, Writing – review & editing. **Alfredo Bol:** Conceptualization, Data curation, Formal analysis, Funding acquisition, Investigation, Methodology, Project administration, Resources, Writing – original draft, Writing – review & editing. **Santiago Aparicio:** Conceptualization, Data curation, Formal analysis, Funding acquisition, Methodology, Project administration, Resources, Software, Supervision, Validation, Visualization, Writing – original draft, Writing – review & editing.

Declaration of competing interest

The authors declare that they have no known competing financial interests or personal relationships that could have appeared to influence the work reported in this paper.
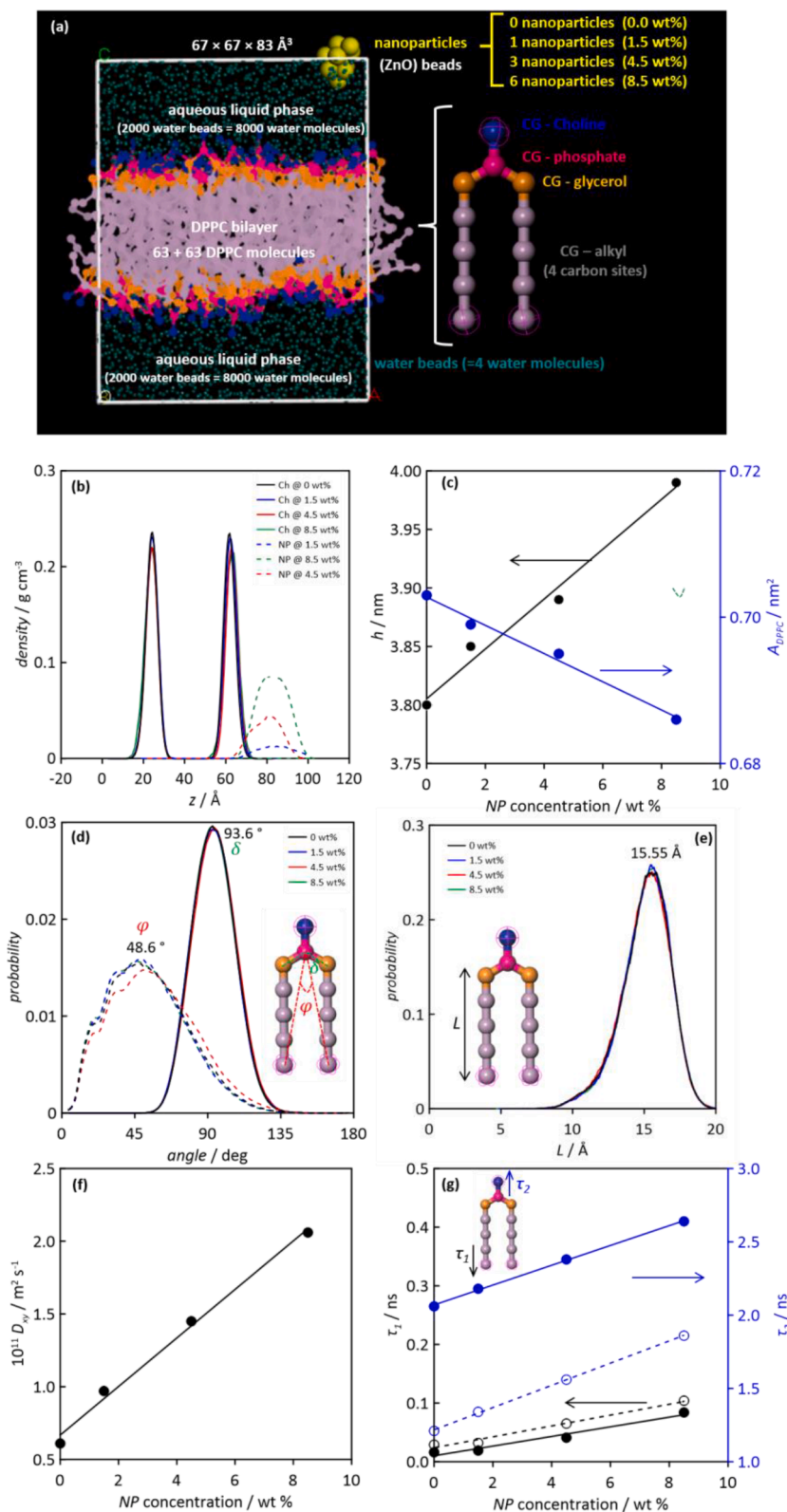
Fig. 19. Results of Coarse Grained MD simulations at 328 K and 1 bar for the interaction of $(ZnO)_{12}$ nanoparticles in aqueous solution at different concentrations (wt %) in contact with a DPPC lipid bilayer. Panel (a) indicates simulation set up as well as molecules arranged in beads for Coarse Graining. Panels: (b) distribution of choline bead (Ch, continuous lines) and (ZnO) beads (NP, dashed lines) in the direction perpendicular to the bilayer; (c) lipid bilayer thickness, h, and area per lipid, A_{DPPC}; (d) distribution of the reported angles in DPPC molecule; (e) distribution of the reported DPPC chain length; (f) DPPC lateral diffusion, D_{xy}; (g) short, τ_1, and long, τ_2, constants form the fit of Rotational Correlation function of the reported vectors to a two exponential decay function.
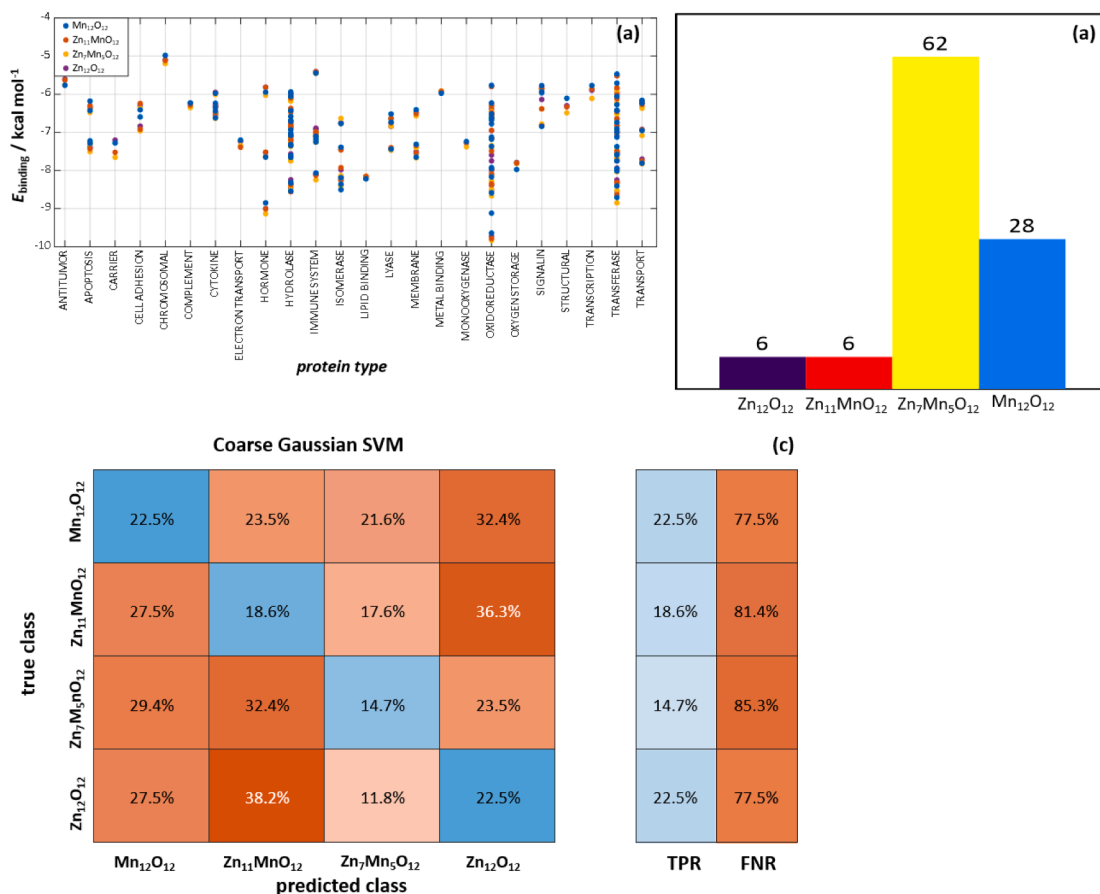
Fig. 20. Docking results for the reported nanoparticles in the selected proteins. (a) Nanoparticle – protein average binding energy ($E_{binding}$), as obtained from the 9-largest binding poses for each protein; (b) nanoparticles frequency of having the largest binding energy for each protein considered; Confussion matriz for the classification learner using coarse gaussian SVM using $E_{binding}$ as the classification criteria also showing True Positive Rates (TPR) and False Negative Rates (FNR). Proteins are classified per type (Table S1, Supplementary Information).

Data availability

Data will be made available on request.

Supplementary materials

Supplementary material associated with this article can be found, in the online version, at doi:10.1016/j.surfin.2024.103965.

References

[1] https://ec.europa.eu/environment/chemicals/nanotech/index_en.htm (2024).
[2] A.S. Abdelsattar, A. Dawoud, M.A. Helal, Interaction of nanoparticles with biological macromolecules: a review of molecular docking studies, Nanotoxicology 15 (2020) 66–95.
[3] D. Wu, R. Zhao, Y. Chen, Y. Wang, J. Li, Y. Fan, Molecular insights into MXene destructing the cell membrane as a no thermal blade, Phys. Chem. Chem. Phys. 23 (2021) 3341–3350.

[4] J. Leitner, V. Bartůněk, D. Sedmidubský, O. Jankovský, Thermodynamic properties of nanostructured ZnO, Appl. Mater. Today 10 (2018) 1–11, https://doi.org/10.1016/j.apmt.2017.11.006.
[5] R. Yue, S.G. Ramaraj, H. Liu, D. Elamaran, V. Elamaran, S. Arya, S. Verma, S. Satapathi, Y. hayawaka, X. Liu, A review of flexible lead-free piezoelectric energy harvester, J. Alloy. Compd. 918 (2022) 165653, https://doi.org/10.1016/j.jallcom.2022.165653.
[6] H. Ahmoum, G. Li, M. Boughrara, R. Gebauer, M.S. Su'ait, K. Tanji, M. Kerouad, Q. Wang, Oxygen vacancy suppress room temperature ferromagnetism of p-type Cu doped ZnO: synthesis and density functional theory, Micro Nanostruct. 167 (2022) 207291, https://doi.org/10.1016/j.micrna.2022.207291.
[7] B. Ludi, M. Niederberger, Zinc oxide nanoparticles: chemical mechanisms and classical and non-classical crystallization, Dalton Trans. 42 (2013) 12554, https://doi.org/10.1039/c3dt50610j.
[8] A. Wibowo, M.A. Marsudi, M.I. Amal, M.B. Ananda, R. Stephanie, H. Ardy, L. J. Diguna, ZnO nanostructured materials for emerging solar cell applications, RSC Adv. 10 (2020) 42838–42859, https://doi.org/10.1039/D0RA07689A.
[9] M. Martínez-Carmona, Y. Gun'ko, M. Vallet-Regí, ZnO nanostructures for drug delivery and theranostic applications, Nanomaterials 8 (2018) 268, https://doi.org/10.3390/nano8040268.
[10] M. Srivastava, A. Srivastava, Electron transport in CO2 adsorbed ZnO nanowire: DFT study, Chem. Phys. Lett. 729 (2019) 17–23, https://doi.org/10.1016/j.cplett.2019.05.014.
[11] B. Ul Haq, First-principles calculations to investigate thermoelectric properties of new monolayers of ZnO, Optik 238 (2021) 166782, https://doi.org/10.1016/j.ijleo.2021.166782.
[12] A. Hamed Mashhadzadeh, M. Fathalian, M. Ghorbanzadeh Ahangari, M. H. Shahavi, DFT study of Ni, Cu, Cd and Ag heavy metal atom adsorption onto the surface of the zinc-oxide nanotube and zinc-oxide graphene-like structure, Mater. Chem. Phys. 220 (2018) 366–373, https://doi.org/10.1016/j.matchemphys.2018.09.016.
[13] P. Nandi, D. Das, Morphological variations of ZnO nanostructures and its influence on the photovoltaic performance when used as photoanodes in dye sensitized solar cells, Sol. Energy Mater. Sol. Cells 243 (2022) 111811, https://doi.org/10.1016/j.solmat.2022.111811.
[14] L. Huang, Enhanced light output of scintillators by ZnO nanorod arrays, Phys. E 142 (2022) 115326, https://doi.org/10.1016/j.physe.2022.115326.

[15] W. Xu, H. Cao, H. Chen, Y. Yang, A. Sarkar, Sensing the cathinone drug concentration in the human body by using zinc oxide nanostructures: a DFT study, Struct. Chem. 32 (2021) 63–68, https://doi.org/10.1007/s11224-020-01611-y.

[16] A. Abbasi, J.J. Sardroodi, A highly sensitive chemical gas detecting device based on N-doped ZnO as a modified nanostructure media: a DFT+NBO analysis, Surf. Sci. 668 (2018) 150–163, https://doi.org/10.1016/j.susc.2017.10.029.

[17] M. Sheikha, M. Paziroftehc, M. Dehghanid, M. Asgharid, M. Rezakazemie, C. Valderrama, J.L. Cortina, Application of ZnO nanostructures in ceramic and polymeric membranes for water and wastewater technologies: a review, Chem. Eng. J. 391 (2020) 123475.

[18] S. Adesoye, ZnO and TiO₂ nanostructures for surface-enhanced Raman scattering-based bio-sensing: a review, Sens. Bio Sens. Res. 37 (2022) 100499, https://doi.org/10.1016/j.sbsr.2022.100499.

[19] V. Gerbreders, M. Krasovska, E. Sledevskis, A. Gerbreders, I. Mihailova, E. Tamanis, A. Ogurcovs, Hydrothermal synthesis of ZnO nanostructures with controllable morphology change, CrystEngComm. 22 (2020) 1346–1358, https://doi.org/10.1039/C9CE01556F.

[20] V. Singh, R. Singh, Simple synthesis of ZnO 3D-hierarchical nanostructures by microfluidics process, J. Mater. Sci. Mater. Electron. 33 (2022) 14837–14846, https://doi.org/10.1007/s10854-022-08403-6.

[21] M.T. Noman, N. Amor, M. Petru, Synthesis and applications of ZnO nanostructures (ZONSs): a review, Crit. Rev. Solid State Mater. Sci. 47 (2022) 99–141, https://doi.org/10.1080/10408436.2021.1886041.

[22] S. Raha, Md. Ahmaruzzaman, ZnO nanostructured materials and their potential applications: progress, challenges and perspectives, Nanoscale Adv. 4 (2022) 1868–1925, https://doi.org/10.1039/D1NA00880C.

[23] B. Ul Haq, S. AlFaify, T. Alshahrani, R. Ahmed, S.A. Tahir, N. Amjed, A. Laref, Exploring optoelectronic properties of ZnO monolayers originated from NaCl- and GeP-like polymorphs: a first-principles study, Results Phys. 19 (2020) 103367, https://doi.org/10.1016/j.rinp.2020.103367.

[24] I.V. Tudose, N. Vrinceanu, C. Pachiu, S. Bucur, P. Pascariu, L. Rusen, E. Koudoumas, M.P. Suchea, Nanostructured ZnO-based materials for biomedical and environmental applications. Functional Nanostructured Interfaces for Environmental and Biomedical Applications, Elsevier, 2019, pp. 285–305, https://doi.org/10.1016/B978-0-12-814401-5.00011-6.

[25] M.J.S. Spencer, Gas sensing applications of 1D-nanostructured zinc oxide: insights from density functional theory calculations, Prog. Mater. Sci. 57 (2012) 437–486, https://doi.org/10.1016/j.pmatsci.2011.06.001.

[26] M.S. Krishna, Detection of carcinogenic heavy metals using ZnO nanoribbons (ZnONRs): ab-initio analysis, Phys. E 142 (2022) 115289, https://doi.org/10.1016/j.physe.2022.115289.

[27] C. Magro, T. Moura, J. Dionísio, P.A. Ribeiro, M. Raposo, S. Sério, Nanostructured metal oxide sensors for antibiotic monitoring in mineral and river water, Nanomaterials 12 (2022) 1858, https://doi.org/10.3390/nano12111858.

[28] I. Kim, K. Viswanathan, G. Kasi, S. Thanakkasaranee, K. Sadeghi, J. Seo, ZnO nanostructures in active antibacterial food packaging: preparation methods, antimicrobial mechanisms, safety issues, future prospects, and challenges, Food Rev. Int. 38 (2022) 537–565, https://doi.org/10.1080/87559129.2020.1737709.

[29] V. Puspasari1, A. Ridhova1, A. Hermawan, M.I. Amal, M.M. Khan, ZnO-based antimicrobial coatings for biomedical applications, Bioprocess. Biosyst. Eng. 45 (2022) 1346–1358, https://doi.org/10.1007/s00449-022-02733-9.

[30] J. El Ghoul, F.F. Alharbi, Simple route synthesis of (Al, Ni) co-doped ZnO nanoparticles and their characterizations, Dig. J. Nanomater. Biostruct. 17 (2022) 549–555, https://doi.org/10.15251/DJNB.2022.172.549.

[31] B. Wang, S. Nagase, J. Zhao, G. Wang, Structural growth sequences and electronic properties of zinc oxide clusters (ZnO)n (n =2-18), J. Phys. Chem. C 111 (2007) 4956–4963, https://doi.org/10.1021/jp066548v.

[32] B. Wang, X. Wang, G. Chen, S. Nagase, J. Zhao, Cage and tube structures of medium-sized zinc oxide clusters (ZnO)n (n=24, 28, 36, and 48), J. Chem. Phys. 128 (2008) 144710, https://doi.org/10.1063/1.2898882.

[33] B. Wang, X. Wang, J. Zhao, atomic structure of the magic (ZnO)60 cluster: first-principles prediction of a sodalite motif for ZnO nanoclusters, J. Phys. Chem. C 114 (2010) 5741–5744, https://doi.org/10.1021/jp908472h.

[34] M. Zhao, Y. Xia, Z. Tan, X. Liu, L. Mei, Design and energetic characterization of ZnO clusters from first-principles calculations, Phys. Lett. A 372 (2007) 39–43, https://doi.org/10.1016/j.physleta.2007.06.070.

[35] A.C. Reber, S.N. Khanna, J.S. Hunjan, M.R. Beltran, Rings, towers, cages of ZnO, Eur. Phys. J. D 43 (2007) 221–224, https://doi.org/10.1140/epjd/e2007-00087-7.

[36] R. Bovhyra, D. Popovych, O. Bovgyra, A. Serednytski, Ab initio study of structural and electronic properties of (ZnO)n "magical" nanoclusters n = (34, 60), Nanoscale Res. Lett. 12 (2017) 76, https://doi.org/10.1186/s11671-017-1848-8.

[37] J.M. Matxain, J.M. Mercero, J.E. Fowler, Ugalde, electronic excitation energies of ZniOi clusters, J. Am. Chem. Soc. 125 (2003) 9494–9499, https://doi.org/10.1021/ja0264504.

[38] A. Dmytruk, I. Dmitruk, I. Blonskyy, R. Belosludov, Y. Kawazoe, A. Kasuya, ZnO clusters: laser ablation production and time-of-flight mass spectroscopic study, Microelectron. J. 40 (2009) 218–220, https://doi.org/10.1016/j.mejo.2008.07.010.

[39] S. Zhang, Y. Zhang, S. Huang, H. Liu, P. Wang, H. Tian, Theoretical investigation of growth, stability, and electronic properties of beaded ZnO nanoclusters, J. Mater. Chem. 21 (2011) 16905, https://doi.org/10.1039/c1jm12061a.

[40] Q. Chen, J. Wang, Structural, electronic, and magnetic properties of TMZn₁₁O₁₂ and TM₂Zn₁₀O₁₂ clusters (TM=Sc, Ti, V, Cr, Mn, Fe, Co, Ni, and Cu), Chem. Phys. Lett. 474 (2009) 336–341, https://doi.org/10.1016/j.cplett.2009.05.006.

[41] W. Pipornpong, B. Kaewruksa, V. Ruangpornvisuti, DFT investigation on molecular structures of metal and nonmetal-doped ZnO sodalite-like cage and their electronic properties, Struct. Chem. 27 (2016) 773–784, https://doi.org/10.1007/s11224-015-0625-5.

[42] P.S. Maddahi, M. Yeganeh, F.B. Baghsiyahi, ZnO nanoparticles as a sensitive platform for detection of nitration in tyrosine and tryptophan: a DFT study, Mater. Chem. Phys. 237 (2019) 121857, https://doi.org/10.1016/j.matchemphys.2019.121857.

[43] B.K. Rao, Site specific interactions of amino acids with (ZnO)12 cluster: density functional approach, J. Biomol. Struct. Dyn. 40 (2022) 13325–13333, https://doi.org/10.1080/07391102.2021.1987327.

[44] J. Cheng, D. Hu, A. Yao, Y. Gao, H. Asadi, A computational study on the Pd-decorated ZnO nanocluster for H2 gas sensing: a comparison with experimental results, Phys. E Low Dimens. Syst. Nanostruct. 124 (2020) 114237, https://doi.org/10.1016/j.physe.2020.114237.

[45] J. Zhang, M. Dolg, ABCluster: the artificial bee colony algorithm for cluster global optimization, Phys. Chem. Chem. Phys. 17 (2015) 24173–24181, https://doi.org/10.1039/C5CP04060D.

[46] M.D. Hanwell, D.E. Curtis, D.C. Lonie, T. Vandermeersch, E. Zurek, G.R. Hutchison, Avogadro: an advanced semantic chemical editor, visualization, and analysis platform, J. Cheminform. 4 (2012) 17, https://doi.org/10.1186/1758-2946-4-17.

[47] J.P. Perdew, K. Burke, M. Ernzerhof, Generalized gradient approximation made simple, Phys. Rev. Lett. 77 (1996) 3865–3868, https://doi.org/10.1103/PhysRevLett.77.3865.

[48] S. Grimme, J. Antony, S. Ehrlich, H. Krieg, A consistent and accurate ab initio parametrization of density functional dispersion correction (DFT-D) for the 94 elements H-Pu, J. Chem. Phys. 132 (2010) 154104, https://doi.org/10.1063/1.3382344.

[49] T. Lu, F. Chen, Multiwfn: a multifunctional wavefunction analyzer, J. Comput. Chem. 33 (2012) 580–592, https://doi.org/10.1002/jcc.22885.

[50] R.F.W. Bader, Atoms in Molecules - a Quantum Theory, Oxford University Press, Oxford, 1990.

[51] A. Aghahosseini, L. Edjlali, S. Jamehbozorgi, M. Rezvani, E. Ghasemi, Theoretical investigations of functionalization of graphene and ZnO monolayers with mercaptopurine at aqueous media: a dispersion-corrected DFT calculations and molecular dynamic simulations, J. Mol. Liq. (2023) 120865, https://doi.org/10.1016/j.molliq.2022.120865.

[52] M. Mohammadzaheri, S. Jamehbozorgi, M.D. Ganji, M. Rezvani, Z. Javanshir, Toward functionalization of ZnO nanotubes and monolayers with 5-aminolevulinic acid drugs as possible nanocarriers for drug delivery: a DFT based molecular dynamic simulation, Phys. Chem. Chem. Phys. 25 (2023) 21492–21508, https://doi.org/10.1039/D3CP01490H.

[53] M. Kurban, Sulfur doping concentration effect on the electronic and structural properties of ZnO nanoparticles: insights from DFTB calculations, J. Chem. Theor. Comput. 1224 (2023) 114112, https://doi.org/10.1016/j.comptc.2023.114112.

[54] M. Saeedimasine, F. Grote, A.P. Lyubartsev, Ab Initio derived classical force field for molecular dynamics simulations of ZnO surfaces in biological environment, J. Phys. Chem. A 127 (2023) 5446–5457, https://doi.org/10.1021/acs.jpca.3c00424.

[55] B. Hourahine, B. Aradi, V. Blum, F. Bonafe, A. Buccheri, C. Camach, C. Cevallos, M.Y. Deshaye, T. Dumitrica, A. Dominguez, et al., DFTB+, a software package for efficient approximate density functional theory based atomistic simulations, J. Chem. Phys. 152 (2020) 124101.

[56] N.H. Moreira, G. Dolgonos, B. Aradi, A.L. da Rosa, T. Frauenheim, Toward an accurate density-functional tight-binding description of zinc-containing compounds, J. Chem. Theor. Comput. 5 (2009) 605–614.

[57] https://materialsproject.org/ Accessed on 2023.

[58] K. Harun, N.A. Slleh, B. Daghfel, M.K. Yaakob, A.A. Mohamad, DFT+U calculations for electronic, structural, and optical properties of ZnO wurtzite structure: a review, Res. Phys. 16 (2020) 102829.

[59] J.M. Rahm, P. Erhart, WulffPack: a Python package for Wulff constructions, J. Open Source Softw. 5 (2020) 1944.

[60] S.J. Marrink, H.J. Risselada, S. Yefimov, D.P. Tieleman, A.H. de Vries, The MARTINI forcefield: coarse grained model for biomolecular simulations, J. Phys. Chem. B 111 (2007) 7812–7824.

[61] R.L.C. Akkermans, N.A. Spenley, S.H. Robertson, COMPASS III: automated fitting of workflows and extension to ionic liquids, Mol. Simul. 47 (2021) 540–551.

[62] J. Hyun, R. Chang, Penetration of C60 into lung surfantant membranes: molecular dynamics simulation studies, Bull. Korean Chem. Soc. 43 (2022) 364–368.

[63] Q. Ying, X. Shi, H. Ding, X. Dai, G. Wan, Y. Qiao, Interactions of borneol with DPPC phospholipid membrane: a molecular dynamics simulation study, Int. J. Mol. Sci. 15 (2014) 20365–20381.

[64] G. Martínez-Rosell, T. Giorgino, G. De Fabritiis, PlayMolecule ProteinPrepare: a web application for protein preparation for molecular dynamics simulations, J. Chem. Inf. Model. 57 (2017) 1511–1516.

[65] O. Trott, A.J. Olson, AutoDock Vina: improving the speed and accuracy of docking with a new scoring function, efficient optimization, and multithreading, J. Comput. Chem. 31 (2010) 455–461.

[66] D. Santos-Martins, S. Forli, M. João Ramos, A. Olson, AutoDock4Zn: an improved autodock force field for small-molecule docking to zinc metalloproteins, J. Chem. Inf. Model. 54 (2014) 2371–2379.

[67] T. Han, F.Y. Meng, S. Zang, X.M. Cheng, J.I. Oh, Band gap and electronic properties of wurtzite – structure ZnO co-doped with IIA and IIIA, J. Chem. Appl. Phys. 110 (2011) 063724.

[68] E.S. Goh, J.W. Mah, T.L. Yoon, Effects of Hubbard term correction on the structural parameters and electronic properties of wurtzite ZnO, Computat. Mater. Sci. 138 (2017) 111–116.

[69] A. Sharma, B.P. Singh, S. Dhar, A. Gonford, M. Spasova, Effect of surface groups on the luminescence property of ZnO nanoparticles synthesized by sol-gel route, Surf. Sci. 606 (2012) L13–L17.

[70] V.I. Korepanov, S.Y. Chan, H.C. Hsu, H.O. Hamaguchi, Phonon confinement and size effect in Raman spectra of ZnO nanoparticles, Heliyon 5 (2019) e01222.

[71] M. Yoshikawa, K. Inoue, T. Nakagawa, H. Ishida, N. Hasuike, H. Harima, Characterization of ZnO nanoparticles by resonant Raman scattering and cathodoluminescence spectroscopies, Appl. Phys. Lett. 92 (2008) 113115.

[72] P. Pandey, M.R. Parra, F.Z. Haque, R. Kurchania, Effects of annealing temperature optimization on the efficiency of ZnO nanoparticles photoanode based dye sensitized solar cells, J. Mater. Sci. Mater. Electron. 28 (2017) 1537–1545.

[73] V.l. Chandraboss, B. Karthikeyan, S. Senthilvelan, Experimental and first principles study of guanine adsorption on ZnO clusters, Phys. Chem. Chem. Phys. 16 (2014) 23461–23475.

[74] M. Chen, T.P. Straatsma, Z. Fang, D.A. Dixon, Structural and electronic property study of $(ZnO)_n$, $n \leq 168$: transition from zinc oxide molecular clusters to ultrasmall nanoparticles, J. Phys. Chem. C 120 (2016) 20400–20418.

[75] Y.M. Hu, C.Y. Wang, S.S. Lee, T.C. Han, W.Y. Chou, G.J. Chen, Identification of Mn-related Raman modes in Mn-doped ZnO thin films, J. Raman Spectrosc. 42 (2011) 434–437.

[76] U. Koch, P.L.P. Popelier, Characterization of C-H-O hydrogen bonds on the basis of the charge density, J. Phys. Chem. 99 (1995) 9747–9754.

[77] R.B. Reed, D.A. Ladner, C.P. Higgins, P. Westerhoff, J.F. Ranville, Solubility of nano-zinc oxide in environmentally and biologically important matrices, Environ. Toxicol. Chem. 31 (2012) 93–99.

[78] T.E. Allen, J.M. Goodman, S. Gutsell, P.J. Russell, Defining molecular initiating events in the adverse outcome pathway framework for risk assessment, Chem. Res. Toxicol. 27 (2014) 2100–2112.

[79] T.M. Abdelghany, A.C. Leitch, I. Nevjestic, I. Ibrahim, S. Miwa, C. Wilson, S. Heutz, M.C. Wright, Emerging risk from "environmentally-friendly" solvents: interaction of methylimidazolium ionic liquids with the mitochondrial electron transport chain is a key initiation event in their mammalian toxicity, Food Chem. Technol. 145 (2020) 111593.

[80] E.M. Curtis, C.K. Hall, Molecular dynamics simulations of DDPC bilayers using LIME: a New coarse-grained model, J. Phys. Chem. B 117 (2013) 5019. -2030.